ELSEVIER

Journal of South American Earth Sciences 23 (2007) 147–175

Journal of
South American
Earth Sciences

www.elsevier.com/locate/jsames

Counterclockwise tectonometamorphic evolution of the Pringles Metamorphic Complex, Sierras Pampeanas of San Luis (Argentina)

Sergio H. Delpino [a,*], Ernesto A. Bjerg [a,b], Gabriela R. Ferracutti [a,b], Aberra Mogessie [c]

[a] *INGEOSUR-Departamento de Geología, Universidad Nacional del Sur, San Juan 670, B8000ICN Bahía Blanca, Argentina*
[b] *Consejo Nacional de Investigaciones Científicas y Técnicas (CONICET), San Juan 670, B8000ICN Bahía Blanca, Argentina*
[c] *Institute of Mineralogy and Petrology, Karl Franzens University Graz, Universitätsplatz 2, A8010 Graz, Austria*

Received 1 December 2003; accepted 1 June 2006

Abstract

The crystalline basement of the Sierra de San Luis, which belongs to the Eastern Sierras Pampeanas in central Argentina, consists of three main units: (1) Conlara, (2) Pringles, and (3) Nogolí metamorphic complexes. In the Pringles Metamorphic Complex, mafic–ultramafic bodies occur as discontinuous lenses along a narrow central belt concordant with the general NNE–SSW structural trend. A metamorphic gradient from granulite to greenschist facies is apparent on both sides of the mafic–ultramafic bodies. This work focuses on the characteristics of the mylonitization overprinted on the mafic–ultramafic intrusives in the Pringles Metamorphic Complex and their gneissic–migmatitic surroundings, both previously metamorphosed within the granulite facies. Petrogenetic grid and geothermobarometry applied to the paragenesis equilibrated during the mylonitic event, together with mineral deformation mechanisms, indicate that mafic and adjacent basement mylonites developed under upper amphibolite transitional to granulite facies metamorphic conditions at intermediate pressures (668–764 °C, 6.3–6.9 kbar, $0.3 < X\mathrm{CO}_2 < 0.7$). However, the following mylonitic assemblages can be distinguished from the external limits of the Pringles Metamorphic Complex to its center: lower amphibolite facies ⇒ middle amphibolite facies ⇒ upper amphibolite transitional to granulite facies. Geothermobarometry applied to mylonitic assemblages indicate a temperature gradient from 555 °C to 764 °C and pressures of 6–7 kbar for the mylonitic event. This event is considered to have developed on a preexisting temperature gradient attributed to the intrusion of mafic–ultramafic bodies. The concentration of sulfides in mylonitic bands and textural relationships provide evidence of remobilization of primary magmatic sulfides of the mafic–ultramafic rocks (+PGM) during the mylonitic event. A lower-temperature final overprint produced brittle fracturing and localized retrogression on mafic–ultramafic minerals and ores by means of a water-rich fluid phase, which gave rise to a serpentine + magnetite ± actinolite association. Concordantly in the adjacent country rocks, fluids channeled along preexisting mylonitic foliation planes produced local obliteration of the mylonitic texture by a randomly oriented replacement of the mylonite mineralogy by a chlorite + sericite/muscovite + magnetite assemblage. Observed mineral reactions combined with structural data and geothermobarometry suggest a succession of tectonometamorphic events for the evolution of the Pringles Metamorphic Complex of Sierra de San Luis, developed in association with a counterclockwise *P–T–d* path. The most likely geological setting for this type of evolution is a backarc basin, associated with east-directed Famatinian subduction initiated in Mid-Cambrian times and closed during the collision of the allochthonous Precordillera terrane in Mid-Ordovician times.

Keywords: Mylonites; Geothermobarometry; *P–T–d*; Counterclockwise; Backarc; Famatinian; Sierras Pampeanas; Argentina

Resumen

La Sierra de San Luis forma parte de las Sierras Pampeanas Orientales situadas en la región central de Argentina. Su basamento cristalino está constituído por tres unidades principales: (1) Complejo Metamórfico Conlara, (2) Complejo Metamórfico Pringues, y (3) Complejo Metamórfico Nogolí. En el Complejo Metamórfico Pringles, los cuerpos máfico-ultramáficos se disponen en una angosta faja

* Corresponding author. Tel.: +54 291 4595101x3061; fax: +54 291 4595148.
E-mail address: sdelpino@criba.edu.ar (S.H. Delpino).

0895-9811/$ - see front matter © 2006 Elsevier Ltd. All rights reserved.
doi:10.1016/j.jsames.2006.09.019

central concordante con la estructura regional NNE–SSW, a ambos lados de la cual se hace evidente un gradiente metamórfico variable entre facies de granulitas y esquistos verdes. En el presente trabajo se presta especial atención a las características de la milonitizacion sobreimpuesta a los intrusivos máfico-ultramáficos y las rocas de caja gnéisicas-migmatíticas adyacentes, ambos tipos litológicos previamente afectados por metamorfismo en facies de granulitas. Las condiciones de estabilidad de las paragénesis equilibradas en el transcurso del evento milonítico analizadas a través de una grilla petrogenética adecuada, las determinaciones geotermobarométricas (668–764 °C, 6.3–6.9 kbar, $0.3 < XCO_2 < 0.7$) y el análisis de mecanismos de deformación en minerales, indican que las milonitas máficas y del basamento adyacente se desarrollaron bajo condiciones metamórficas en facies de anfibolita alta transicional a granulita y a presiones intermedias. Sin embargo, las siguientes asociaciones miloníticas pueden identificarse desde los límites externos del Complejo Metamórfico Pringles hacia su parte central: facies anfibolitas baja ⇒ facies anfibolitas media ⇒ facies anfibolitas alta transicional a granulitas. La geotermobarometría aplicada a estas asociaciones miloníticas, indican un gradiente térmico de 555 °C a 764 °C y presiones en el rango 6–7 kbar para el evento milonítico. Se considera que este evento milonítico tuvo lugar sobre un gradiente térmico desarrollado previamente y atribuido a la intrusión de los cuerpos máfico-ultramáficos. La concentración de sulfuros en las bandas miloníticas y las relaciones texturales, proveen evidencias indudables de la removilización de los sulfuros magmáticos y elementos del grupo del platino de las rocas máficas-ultramáficas durante el evento milonítico. Un evento póstumo de baja temperatura dio lugar a un fracturamiento frágil y a la retrogradación localizada de los minerales máfico-ultramáficos y de las menas asociadas, por medio de una fase fluída rica en agua evidenciada por el desarrollo de la asociación serpentina + magnetita ± actinolita. Concordantemente, en las rocas de caja adyacentes los fluídos canalizados a través de los planos de foliación miloníticos preexistentes, dieron lugar a la obliteración localizada de la textura milonítica a través del reemplazo masivo de su mineralogía por la asociación clorita + sericita/moscovita + magnetita. Sobre la base de las reacciones minerales observadas en combinación con los datos estructurales y geotermobarométricos, se propone la sucesión de eventos tectonometamórficos acaecidos en el Complejo Metamórfico Pringles de la Sierra de San Luis, desarrollados en asociación con una trayectoria *P–T–d* antihoraria. El ambiente geotectónico más probable para una evolución de estas características es una cuenca de retroarco, cuya apertura podría vincularse con la subducción Famatiniana (dirigida hacia el Este) iniciada en el Cámbrico Medio, y su cierre relacionado con la colisión del terreno alóctono de Precordillera en el Ordovícico Medio.

Palabras clave: Milonitas; Geotermobarometría, *P–T–d*; Antihorario; Retroarco; Famatiniano; Sierras Pampeanas; Argentina

1. Introduction

The Sierras Pampeanas Range, located in central western Argentina, can be divided on the basis of differences in lithologic composition and magmatic–metamorphic evolution into two contrasting units: the Western and Eastern Sierras Pampeanas (Caminos, 1973, 1979; Dalla Salda, 1987). This range formed part of the western margin of Gondwana during the Late Proterozoic–Early Paleozoic, and four geological cycles (see; Pankhurst and Rapela, 1998) intervened in its formation: (1) Pampean (Neoproterozoic–Late Cambrian), (2) Famatinian (Early Ordovician–Early Carboniferous), (3) Gondwanian (Early Carboniferous–Early Cretaceous), and (4) Andean (Early Cretaceous–present).

Located between latitudes 32°–34°S and longitudes 66°–68°W, the Sierra de San Luis represents the southernmost exposure of the Eastern Sierras Pampeanas. According to Sims et al. (1997) and Hauzenberger et al. (2001), the crystalline basement of the Sierra de San Luis (Fig. 1) consists of three main units, from east to west: (1) the Conlara Metamorphic Complex, comprising mainly high-grade gneisses and migmatites; (2) the Pringles Metamorphic Complex, which varies in metamorphic grade from greenschist to granulite facies and comprises phyllites, micaschists, gneisses, migmatites, intercalated mafic–ultramafic rocks, and tonalitic–granodioritic bodies and pegmatites; and (3) the Nogolí Metamorphic Complex, consisting mainly of migmatitic and high-grade gneisses with amphibolite lenses.

The Pringles Metamorphic Complex is clearly distinct from the other units due to the change in metamorphic grade, the occurrence of metabasites within a sequence of quartz–feldspathic and pelitic metasediments, and the presence of a widespread mylonitization event that affects all lithological types and imprints the dominant structural pattern onto this region. These contrasting characteristics, in addition to the differences in the structural configurations (von Gosen, 1998; Sims et al., 1998; Delpino et al., 2001; González et al., 2002), indicate that the tectonometamorphic evolution of the Pringles Metamorphic Complex must have been, at least temporarily, independent of the evolution of the Conlara and Nogolí metamorphic complexes located to the east and west, respectively. Thus, a better knowledge of the geology of this region is essential when attempting to reconstruct the geological history of the Sierra de San Luis and establish correlations with the neighboring areas of the Sierras Pampeanas.

Given their significance in the reconstruction of the tectonometamorphic evolution, the characteristics of the mylonitization event overprinted on the mafic–ultramafic intrusives and their high-grade gneissic–migmatitic surroundings in a selected area of the Pringles Metamorphic Complex represent the main focus of this work (Fig. 1). We made several detailed cross-sections perpendicular to the general trend of the mafic–ultramafic bodies and the main penetrative structural elements between Las Aguilas and El Fierro localities (Fig. 1). We then compare the recognized petrological, structural,

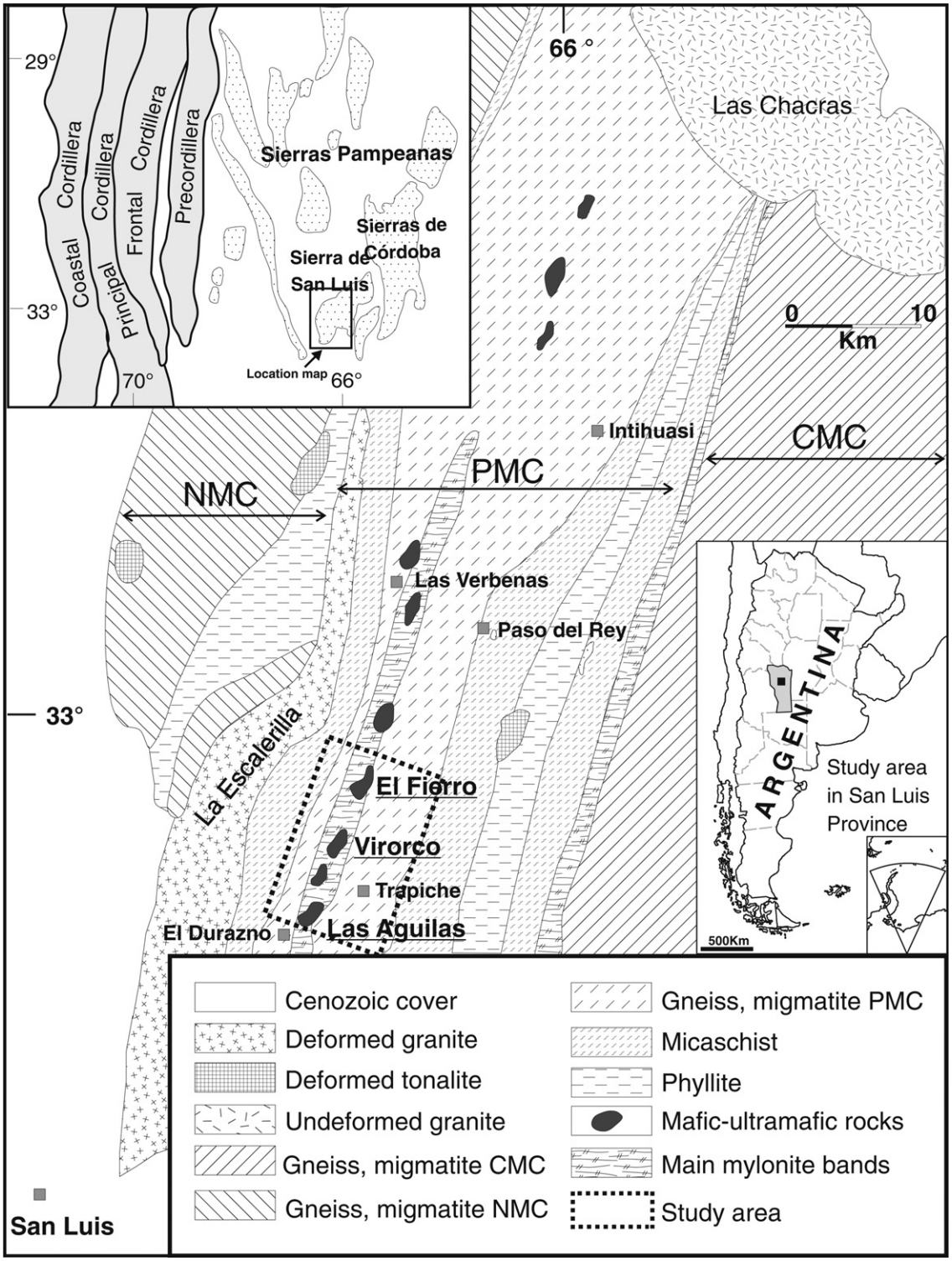

Fig. 1. Simplified geological map of Sierra de San Luis, Sierras Pampeanas, Argentina, based on Llambías et al. (1998) and von Gosen and Prozzi (1998). NMC, Nogolí Metamorphic Complex; PMC, Pringles Metamorphic Complex; CMC, Conlara Metamorphic Complex. The inset shows the regional context of the Sierras Pampeanas. Rectangle indicates the area of study.

and physical characteristics in this central sector with others obtained for the mylonitic rocks located close to the edges of the complex (e.g., von Gosen, 1998; Hauzenberger et al., 2001).

Probably because detailed studies of this deformation event are lacking, significant controversy still exists regarding the timing and metamorphic grade at which the mylonitization event occurred. González Bonorino (1961),

Cucchi (1964), and Sabalúa et al. (1981) were among the first to work on the mylonitization process affecting the mafic–ultramafic bodies and their country rocks in the Pringles Metamorphic Complex. More recently, a broad spectrum of physical conditions, varying from greenschist facies (Brogioni, 1994; Brogioni and Ribot, 1994; von Gosen and Prozzi, 1998) to amphibolite facies (Brogioni, 1992; Malvicini and Brogioni, 1993, 1996; Hauzenberger et al., 1997, 1998, 2001; Delpino et al., 2002), have been attributed to the mylonitization event. Its temporal relationships with other tectonometamorphic events operating in this region are not clear, probably due to the disparities in interpretations of the physical conditions of deformation and the structures reported by different authors (Sims et al., 1998; Hauzenberger et al., 1998, 2001; von Gosen and Prozzi, 1998; Delpino et al., 2001, 2002; Brogioni, 2001).

In response to these discrepancies, this contribution aims to provide a detailed petrographic–microstructural analysis, combined with essential structural and petrological studies, to perform a reliable evaluation of the physical conditions of development of this significant event and its implications for the tectonometamorphic history of the region. The relationships of other geological processes with the mylonitic event are also discussed in detail. Previous works have proposed a postmagmatic remobilization of sulfides + platinum group minerals due to hydrothermal fluids channeled along the shear zones (Malvicini and Brogioni, 1993; Bjerg et al., 1997; Felfernig et al., 1999), but textural evidence linking the remobilization in the basement and mafic–ultramafic rocks with a given tectonic event are scarce (Ferracutti and Bjerg, 2002; Delpino et al., 2002). We consider the relationships of this and other geological processes with the mylonitic event herein.

On the basis of the results of the present and previous works, we present a succession of tectonometamorphic events along a defined *P–T–d* path, as well as the most probable tectonic setting in which it took place.

2. Geotectonic setting

Most authors have suggested Late Precambrian–Early Paleozoic ages for the Sierras Pampeanas basement and associated granitoids. The most recent geochronological studies (Sims et al., 1998; Rapela et al., 1998; Pankhurst et al., 1998; von Gosen et al., 2002; Sato et al., 2002, 2003) indicate that the majority of the geological events took place during the Pampean and Famatinian cycles.

According to Rapela et al. (1998), Early Cambrian (~530 Ma) reconstruction of the proto-Andean margin of South America is characterized by the formation of a passive margin sedimentary basin when subduction of oceanic crust started, forming an accretionary prism and a calc-alkaline volcanic arc along the eastern edge of the Sierras Pampeanas. The subsequent closure of this ocean due to collision of a microcontinent (Pampean terrane) marked the onset of the Pampean Orogeny (Aceñolaza and Toselli, 1976) during early Middle Cambrian times, followed by extensional collapse in the Late Cambrian at the end of the Pampean orogenic cycle.

The Famatinian orogenic cycle, a major accretional and orogenic episode, started with subduction along the new Cambrian proto-Pacific margin (~490 Ma; Pankhurst and Rapela, 1998; Dalla Salda et al., 1992). Subsequent events may be grouped into a prolonged event termed the Famatinian Orogeny (Aceñolaza and Toselli, 1976). Dalla Salda et al. (1992) suggest that this orogeny culminated with the collision of Laurentia and Gondwana in the Middle Ordovician (480–460 Ma). In agreement with the proposal of Dalla Salda et al. (1992), Ramos et al. (1998) postulate that the beginning of the collision between the protomargin of Gondwana and the Cuyania composite terrane (Precordillera terrane of Astini et al., 1995) derived from Laurentia (Ramos et al., 1986; Astini et al., 1995) occurred in the Mid-Ordovician (470–460 Ma). The main Famatinian orogenic phase was followed by a period of extensional collapse and the emplacement of fracture-controlled, undeformed Devonian–Early Carboniferous granitoids (e.g., Brogioni, 1993; Lira and Kirschbaum, 1990; Rapela et al., 1991; Pinotti et al., 1996; López de Luchi, 1996; Llambías et al., 1998).

A new subduction episode developed to the west of the Precordillera, related to the collision of another terrane (Chilenia; Ramos et al., 1984; see also Astini, 1996), was associated with the broadly coeval intrusion of within-plate plutons in the Gondwana foreland (Pankhurst and Rapela, 1998).

3. The Pringles Metamorphic Complex: petrological and structural background

In the Pringles Metamorphic Complex, mafic–ultramafic bodies occur as discontinuous lenses along a narrow central belt concordant with the general NNE–SSW structural trend. According to Mogessie et al. (1994, 1995, 1998), they are composed of orthopyroxene + clinopyroxene + hornblende + plagioclase + sulfides ± olivine ± phlogopite ± Cr-spinel ± platinum group minerals, with accessories such as apatite. On both sides of the mafic–ultramafic bodies, a metamorphic gradient from granulite to greenschist facies is apparent (Delpino et al., 2002). Granulite facies country-rock assemblages (garnet + cordierite + sillimanite + biotite + k-feldspar + plagioclase + quartz + rutile + ilmenite ± orthopyroxene) near mafic–ultramafic bodies grade toward both extremes to the amphibolite facies assemblage (garnet + biotite + muscovite + plagioclase + quartz ± staurolite ± sillimanite ± chlorite) and the easternmost part of the Pringles Metamorphic Complex to the greenschist facies assemblage chlorite + biotite + muscovite + quartz + plagioclase + k-feldpar (Hauzenberger et al., 2001). The granulite facies metamorphism reached by the adjacent country-rocks has been attributed to the intrusion of mafic–ultramafic bodies into a greenschist or amphibolite facies metamorphic sequence

(González Bonorino, 1961; Hauzenberger, 1997; Sims et al., 1998; Hauzenberger et al., 1998; von Gosen and Prozzi, 1998). According to Hauzenberger et al. (2001), the volume of mafic lenses estimated through geophysical methods by Kostadinoff et al. (1998a,b) are great enough to produce the observed granulite facies rocks.

The structure of the Pringles Metamorphic Complex has been discussed in detail by von Gosen and Prozzi (1996, 1998) and Delpino et al. (2001). von Gosen and Prozzi (1998) indicate that fabrics comparable to the D_{x1} to D_{x3} deformations (where "x" refers to pre-Famatinian deformational events) described for the Nogolí Metamorphic Complex also appear in the Pringles Metamorphic Complex. However, neither the description nor locations of such fabrics are indicated by von Gosen and Prozzi (1996, 1998). von Gosen and Prozzi (1998) describe a steeply inclined to subvertical foliation (S_{F2}, where "F" refers to Famatinian deformational events) with a NNE–SSW trend, associated with fold structures (F_{F2}) with axes variably plunging to the NNE or SSW. In some parts, they also recognize an older foliation in the amphibolites, recorded by aligned long axes of amphibole and folded around F_{F2} fold structures (directly related to the tight F_{F2} folding in the metasediments). According to these authors, an intense migmatization of the basement rocks occurred after D_{F2}. The formation of migmatites interferes with F_{F3} fold structures around steeply inclined to vertical axes. The D_{F2} to D_{F3} history was accompanied by high-grade metamorphism. These authors attribute the formation of mylonite zones to a post-Famatinian (D_1) compressive event. The mylonite foliation (S_{my}) strikes NNE–SSW and is vertical or steeply dipping to the east. According to these authors, S_{my} follows the Famatinian S_{F2} foliation, and the displacement mostly follows preexisting planes. Mylonitization is attributed to WNW–ESE compression under greenschist facies conditions.

Delpino et al. (2001) propose that three tectonometamorphic events have taken place in the Pringles Metamorphic Complex: T_1–M_1, prior to the intrusion of the mafic–ultramafic bodies, recognizable only due to compositional layering (Ly, Fig. 2a), preserved only in sectors protected from the mylonitization event (T_3), and affected by T_2, for which the accompanying metamorphism (M_1) reached upper greenschist or amphibolite facies (González Bonorino, 1961; Hauzenberger, 1997; Sims et al., 1998; Hauzenberger et al., 1998; von Gosen and Prozzi, 1998); T_2–M_2, a second deformational event (T_2) well represented in sectors of the basement protected from the subsequent mylonitization (T_3), characterized by very tight folding (F_2) with steeply plunging axes (b_2), and associated with an axial plane foliation (S_2, Fig. 2b), which develops on rocks metamorphosed within the granulite to amphibolite/upper greenschist facies (M_g to M_1) after the emplacement of the mafic–ultramafic rocks and migmatization of the neighboring basement rocks; and T_3–M_3, in which T_3 gives rise to a several km wide shear zone affecting mafic–ultramafic bodies and country-rocks of the Pringles Metamorphic Complex. T_3 produced an intense mylonitization of the whole sequence (which varies in bands trending NNE–SSW) giving rise to protomylonites and mylonites with gradual contacts, and originated folds with subhorizontal axes and a new foliation ($S_m = S_3$, Fig. 2c). As we mentioned previously, the metamorphic conditions of the M_3 event remain a matter of debate, which we discuss further.

4. Methodology

Oriented samples of mafic–ultramafic rocks and gneissic–migmatitic country-rocks were collected between El Fierro and Las Águilas localities (Fig. 1). Given that the shear zone shows an inhomogeneous distribution of deformation, the less deformed specimens of both rock types are identified, which enables the partial recognition of the mineral associations and textural characteristics of the pre-mylonitization protoliths and tracking of the mineralogical and fabric changes undergone by rocks with increasing deformation.

A detailed petrographic-microstructural study of selected representative samples was performed. Polished thin sections were investigated by a combination of transmitted and reflected light microscopy, electron microprobe, and scanning electron microscope (SEM) analysis. The mineral analyses were carried out at the Institute of Mineralogy und Petrology, University of Graz (Austria), with a JEOL 6310 SEM equipped with a LINK ISIS energy dispersive system and a MICROSPEC wavelength dispersive system. Standard analytical conditions for silicates were set to an

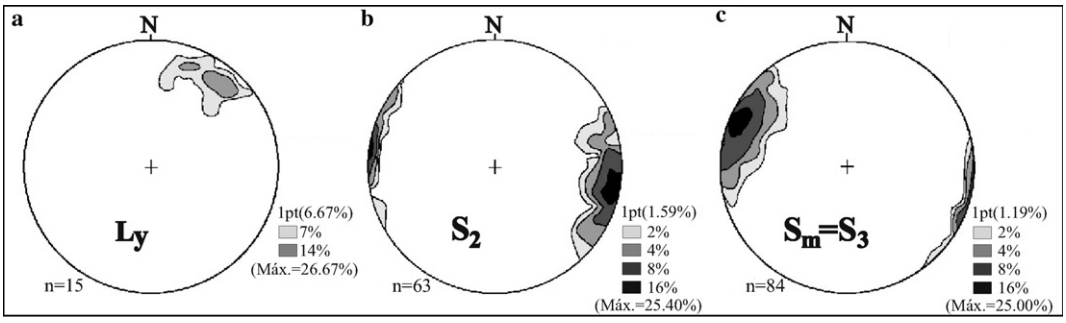

Fig. 2. Density stereograms of three main recognized planar structures in the study area: (a) Ly = compositional layering (T_1 event); (b) S_2 = foliation (T_2 event); and (c) $S_m = S_3$ = mylonitic foliation (T_3 event). Equal area lower-hemisphere projection.

accelerating voltage of 15 kV and a beam current of 5 nA. Matrix corrections of silicates were made using ZAF. The following standards were used: Si, K: adular; Al: andalusite; Fe, Mg: garnet or olivine; Ca, Ti: titanite; Mn: tephroite; Zn: gahnite; and Cr: synthetic Mg-chromite. Detection limits in these routine analyses vary from 0.05 to 0.1 wt.% for the MICROSPEC wavelength dispersive system and 0.1 to 0.5 wt.% for the LINK ISIS energy dispersive system. Relicts and recrystallized and neoformed minerals were analyzed with careful examinations of each phase for the presence of chemical zoning.

Physical conditions of deformation were evaluated through internally consistent geothermobarometry and the construction of a suitable petrogenetic grid for the mineral associations equilibrated during the mylonitic event.

5. Petrographic–microstructural analysis

5.1. Basement mylonites

The basement adjacent to mafic–ultramafic bodies of the CB are mylonitized migmatitic gneisses consisting of garnet + cordierite + sillimanite + biotite + k-feldspar + plagioclase + quartz ± orthopyroxene, plus zircon + rutile + opaque minerals as the main accessory minerals. Deformation is strongly partitioned at the map scale and leads to two types of deformed rocks: S/C protomylonites and banded mylonites.

5.1.1. S/C protomylonites

S/C protomylonites are coarse- to medium-grained light rocks that preserve a characteristic gneissic texture. The protolith of the S/C protomylonites are migmatitic gneisses that have developed an anastomosing to rough disjunctive foliation (Twiss and Moores, 1992) due to mylonitization. Biotite laths, sillimanite, and opaque minerals mainly constitute the cleavage domains. Mono- or polymineralic lenticular to sigmoidal microlithons are composed essentially of k-feldspar, plagioclase, quartz, cordierite, garnet, coarse sillimanite, and biotite. Hauzenberger et al. (2001) document the presence of orthopyroxene, a phase not observed in the samples collected for this work.

Microscopically, the protomylonites show a typical S/C fabric (Fig. 3a), with cleavage domains wrapping around individual porphyroclasts or polyphase microlithons.

Quartz forms ribbons elongated parallel to the mylonitic foliation, constituted by recrystallized polygonal or irregular new grains with straight or sutured contacts and maximum sizes of around 300 μm (Figs. 3a, b, and d). Most quartz grains develop a good crystallographic preferred orientation (Figs. 3a–d).

K-feldspar appears as individual porphyroclasts or constitutes polyphasic microlithons, which usually are composed of k-feldspar with subordinated quartz (Fig. 3b). Despite the mylonitization imprint, microlithons preserve some leucosome characteristics of migmatitic gneisses prior to the mylonitic event. Within these lenses, k-feldspar occurs as coarse, subhedral to anhedral crystals, generally forming triple junctions and lacking any shape or crystallographic preferred orientation (Fig. 3c). The k-feldspar crystals are slightly perthitic and occasionally poikilitic, with inclusions of rounded plagioclase and quartz at their centers (Figs. 3b and c). Only small, interstitial fragments or myrmekitic intergrowths (with poikilitic inclusions) remain as evidence of former plagioclase crystals. In the center of the lenses, k-feldspar crystals show undulatory extinction and evidence of incipient recrystallization (bulging giving rise to slightly serrated mutual contacts) (Fig. 3c). Coarse biotites are interstitial or fill intracrystalline fractures. Although some very small, rounded or subhedral biotite crystals have the appearance of original poikilitic inclusions, most biotite inclusions can be related to thin fractures, also filled with brown-biotite and extending toward k-feldspar crystal edges (Fig. 3c). Within these lenses, scarce, interstitial, coarse quartz grains with undulatory extinction occur (Fig. 3b). However, small, rounded quartz poikilitic inclusions within k-feldspar crystals are optically strain free (Figs. 3b and c). Near the borders of the lenses, quartz shows intense recrystallization, giving rise to arrangements of polygonal grains that extend in ribbons toward the adjacent fine-grained matrix (Fig. 3b).

Outside the best preserved microlithons, k-feldspar porphyroclasts have irregular or rounded shapes and usually show undulatory to patchy extinction (Figs. 3a–d). Reddish-brown biotites usually fill internal microfractures and crystallize at their pressure shadows (Figs. 3a–d). Most k-feldpar porphyroclasts show serrated grain boundaries due to recrystallization along their margins. Recrystallized grains are in contact with porphyroclasts through high-angle boundaries, and no subgrains were observed. Recrystallized grains form aggregates of small (up to 50 μm), irregular to polygonal new grains. Aggregates usually extend as thin ribbons parallel to the foliation and are limited on both sides by coarser quartz ribbons (Fig. 3d). In some cases, small, individual porphyroclasts are entirely surrounded by a fine-grained recrystallized matrix and show lensoidal shapes.

Plagioclase occurs as individual porphyroclasts (up to 5×3 mm) or constitutes polymineralic lenticular to sigmoidal microlithons. Porphyroclasts underwent intense intracrystalline deformation, with microfractures, undulatory or patchy extinction, deformation bands, bending of the primary twinning, and secondary twinning (Fig. 3d). Porphyroclasts are irregular or rounded and often equidimensional. No remarkable flattening of relict grains is present, and subgrains are absent or very scarce. At the contacts with k-feldspar, myrmekitic intergrowths are frequent. Plagioclase porphyroclasts show recrystallization at their edges, usually extending into their pressure shadows (Fig. 3d). Small and irregular recrystallized grains (up to 220 μm) are in mutual contact through sutured boundaries. Recrystallized grains extend away from the porphyroclast tails, forming ribbons of smaller thickness and grain size than those of the adjacent quartz ribbons (Fig. 3d).

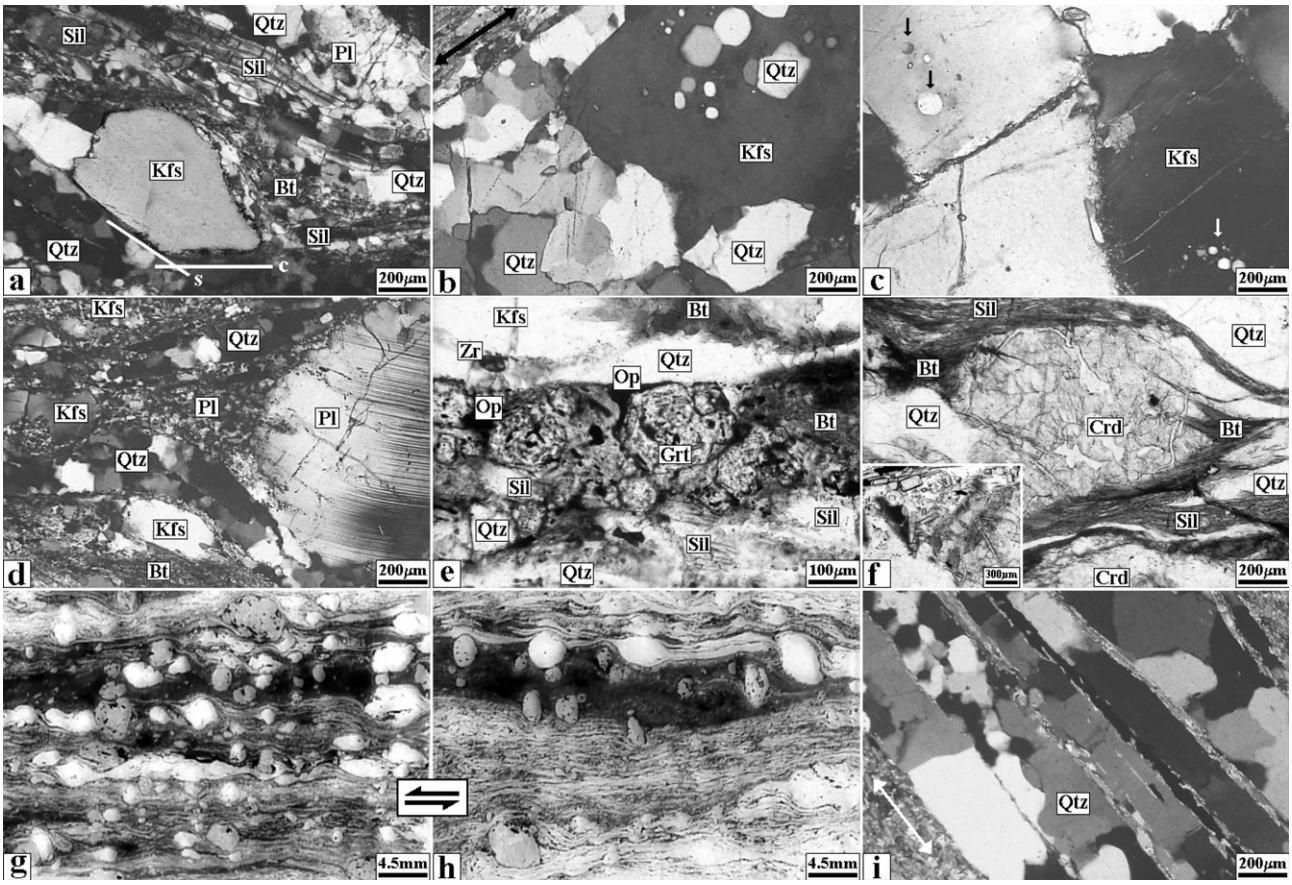

Fig. 3. Photomicrographs of the basement S/C protomylonites (a–f) and mylonites (h–i) from the central sector of the Pringles Metamorphic Complex. All samples normal to foliation and parallel to the stretching lineation. Outcrop orientation of the mylonitic foliation (S_3) is shown in Fig. 2c. (a) General aspect of S/C protomylonites. Observe the C (subhorizontal in the photograph) and S (dipping to right) planes, marked mainly by quartz ribbons, long prismatic sillimanite, and biotite, sweeping around mono- or poliphasic microlithons composed of k-feldspar with subordinated quartz and plagioclase. The S/C microstructure and stair-stepping in k-feldspar porphyroclast (σ_b-structure) indicate a top to W–NW sense of displacement. Crossed nicols. (b) Detail of a preserved k-feldspar and quartz microlithon. Weak intracrystalline deformation in coarse k-feldspar and quartz relict crystals and strain-free quartz inclusions in feldspar. Note increasing quartz deformation toward the biotite-rich mylonitic matrix (top left) and formation of quartz ribbons, composed of coarse, polygonal new grains, meeting at 120° triple junctions. Double arrow, mylonitic foliation. Crossed nicols. (c) Detail of the interior of an almost monophasic (k-feldspar) microlithon preserving part of the rock texture (leucosome) prior to mylonitization. Coarse, subhedral relict k-feldspar crystals form triple junctions and enclose rounded biotite and quartz inclusions (arrows). Crystals show only weak intracrystalline deformation (undulatory extinction) and evidence of incipient grain boundary mobility. Intergranular spaces and internal microfractures filled by neoformed biotite. Crossed nicols. (d) Rounded, bent plagioclase porphyroclast with recrystallized tails. Primary twins have been locally removed by grain boundary migration. Coarse-grained quartz ribbons sweep around plagioclase and k-feldspar (center left) porphyroclasts and delimit finer-grained plagioclase and k-feldspar ribbons. Crossed nicols. (e) Small garnet grains, products of disruption and distribution along mylonitic folia of bigger garnet prophyroclasts. Crystalline phases and enclosed matrix components indicate these fragments grew during the mylonitic event. Plane polarized light. (f) Intensively altered (pinitized) cordierite porphyroclast surrounded by neoformed biotite and sillimanite needles. Crystallization of coarser biotite at porphyroclast tails. Inset (bottom left) shows a detail of a porphyroclast pressure shadow with crystallization of prismatic sillimanite and biotite within extension sites. Note long, prismatic, sillimanite crystals extending into the interior of the porphyroclast. Plane polarized light. (g and h) Scanned thin sections showing general aspect of basement mylonites. Matrix in the light bands composed of coarse quartz ribbons and recrystallized feldspars; dark bands of neoformed biotite dominate. Predominant rounded or elliptic shapes in feldspar porphyroclasts. Note shrinkage and rounding of garnet porphyroclast in biotite-dominated dark folia. Kinematic indicators of σ and δ type in feldspars and garnet and asymmetric and drag folding of quartz ribbons indicate top to W–NW vergence during the T_3 event. (i) Quartz ribbons showing varied internal textural arranges. Polycrystalline ribbons contain blocky quartz with grain boundaries subperpendicular to ribbon's longest dimension; polycrystalline ribbon with large subequant quartz grains contact through sutured boundaries, comparable to Types 3 and 4 of Boullier and Bouchez (1978), respectively. Double arrow, mylonitic foliation. Crossed nicols. Mineral names abbreviated according to Bucher and Frey (1994).

Recrystallization occurs mainly along intracrystalline fractures or at deformation band limits. Breakdown of plagioclase to neoformed biotite during deformation is also evident. Biotite commonly replaces plagioclase crystals at their edges and internal fractures and crystallizes in porphyroclast pressure shadows.

Poikilitic garnets show irregular shapes and sizes in the range 1.5–3 mm and partially or totally enclose quartz or quartz + plagioclase. Garnet grains are often disrupted and small fragments redistributed along the mylonitic foliation (Fig. 3e). These small garnet fragments tend to develop crystalline external faces and incorporate matrix

components (mainly opaque phases and biotite) as poikilitic inclusions. Garnet grains show internal fracturing, usually sealed by biotite and opaque minerals. The same mineral association also crystallizes in the pressure shadows developed during the mylonitic event. In these locations, biotite and opaque minerals do not show intracrystalline deformation.

Sillimanite is a very abundant phase in S/C protomylonites, with two different types of crystals: porphyroclasts and neoformed needles. The porphyroclasts appear as rectangular, square or long prismatic crystals. Most show fractures almost perpendicular to their long dimension and microboudinage. Disrupted microboudins are often redistributed following mylonitic foliation and, together with long prismatic crystals, depict the S and C planes of S/C structures (Berthe et al., 1979) (Fig. 3a). Large porphyroclasts usually show pressure shadows, and some asymmetric rhomboidal fragments resemble the shape of sigmoidal mica-fishes.

Most very abundant neoformed sillimanites appear in the form of aggregates of fine needles following the mylonitic foliation and preferentially replacing or mantling cordierite (Fig. 3f), k-feldspar, and plagioclase porphyroclasts. Acicular prisms and needles with random orientations also can be observed in the interior of cordierite porphyroclasts or parallel to foliation aggregates that partially penetrate the grains concordant with the mylonitic matrix. Small, euhedral, neocrystallized sillimanite crystals with random orientations are often observed in the pressure shadows of altered cordierite crystals (Fig. 3f, inset). Abundant sillimanite needle aggregates commonly develop in high-strained faces of porphyroclasts (e.g., where two k-feldspar porphyroclasts are in mutual contact).

Cordierite is abundant in the S/C protomylonite and occurs, without exception, entirely retrogressed (pinitized, Fig. 3f). Hauzenberger et al. (2001) report the presence of partially preserved fragments of fresh cordierite crystals within the mylonitic zone studied herein, which we did not identify. Neoformed biotite and sillimanite more often form a mantle around cordierite clasts or crystallize within their pressure shadows (Fig. 3f).

Biotite is mainly associated with mylonitic foliation (S and C planes) and extension sites (Figs. 3a, d–f). Coarse biotite crystals principally occur in intracrystalline fractures, pulled apart grain fragments, or pressure shadows of almost all relict grains (garnet, plagioclase, k-feldspar, cordierite, sillimanite), as well as interstitially in the best preserved polyphasic microlithons. Some coarse tabular crystals in strongly mylonitized bands show bending and fracturing. Zircon inclusions with well-developed pleochroic haloes can be observed in some crystals. However, most biotite crystals lack intracrystalline deformation and replace relict phases (essentially k-feldspar, garnet, cordierite, and plagioclase). Fine-grained matrix biotites (up to 200 μm) and coarse-grained biotites (up to 450 μm) crystallized in extension sites are reddish brown, except for biotites replacing cordierites, which have a distinctive green-brownish color.

Zircon, oxides, pyrrhotite, and chalcopyrite constitute the main accessory phases. The modal amount of opaque minerals reaches 1%. They occur mainly in the porphyroclast pressure shadows and as neocrystallized grains within the matrix (Fig. 3e), in both cases generally associated with biotite. Oxides and, in lower proportions, anhedral to subhedral sulfides (pyrrhotite and chalcopyrite) have been recognized filling intracrystalline fractures of silicates. Oxides are ilmenite and magnetite with sizes that reach up to 550 μm, whereas the sulfide maximum size is approximately 130 μm.

5.1.2. Mylonites

Hand specimens of mylonites are banded rocks with alternating light and dark domains (Figs. 3g–h), which, according to Twiss and Moores (1992), can be classified as a compositional foliation. Dark bands are composed of a fine- to medium-grained, biotite-bearing matrix, usually enclosing individual garnet, plagioclase, or k-feldspar porphyroclasts. Light bands either preserve a similar textural appearance and assemblage as the S/C protomylonites or more often show a fine lamination consisting of alternating bands of recrystallized quartz and feldspar grains. Thus, depending on the location of the sample, mylonites show dissimilar aspects due to differences in the deformation intensity (heterogeneously distributed in bands) and variations in the local deformation conditions (modal composition of the protolith, circulation of fluids), which are common features in shear zones.

Microscopically, light bands usually preserve the mineralogy and textures observed in S/C protomylonites and, as a consequence, the mineral phases of the protolith. In contrast, in the dark bands, a matrix of recrystallized and neocrystallized phases predominates, enclosing individual porphyroclasts or polyphase lenses of relict protolithic minerals. Thus, textural differences are obvious for the same phase depending on the location within the sample (light or dark bands).

Quartz is present in the form of large elongate ribbons and lenses consisting entirely of recrystallized grains. The ribbons mark the mylonitic foliation, wrap around other phases, and are frequently asymmetrically folded (drag folds, quarter folds, Figs. 3i and 4g–h). Ribbons or lenses can consist of (1) aggregates of irregular new grains with sutured boundaries, (2) subpolygonal new grains with slightly curved or straight limits forming 120° triple junctions, or (3) elongated (often referred to as blocky) new grains of up to 850 μm, which constitutes the whole ribbon width, laterally in contact with the neighboring grains through straight or lobated boundaries at a high-angle or normal to the long dimension of the ribbon (Figs. 3i and 4h). The recrystallized grains show scarce or null intracrystalline deformation and often develop a good crystallographic preferred orientation

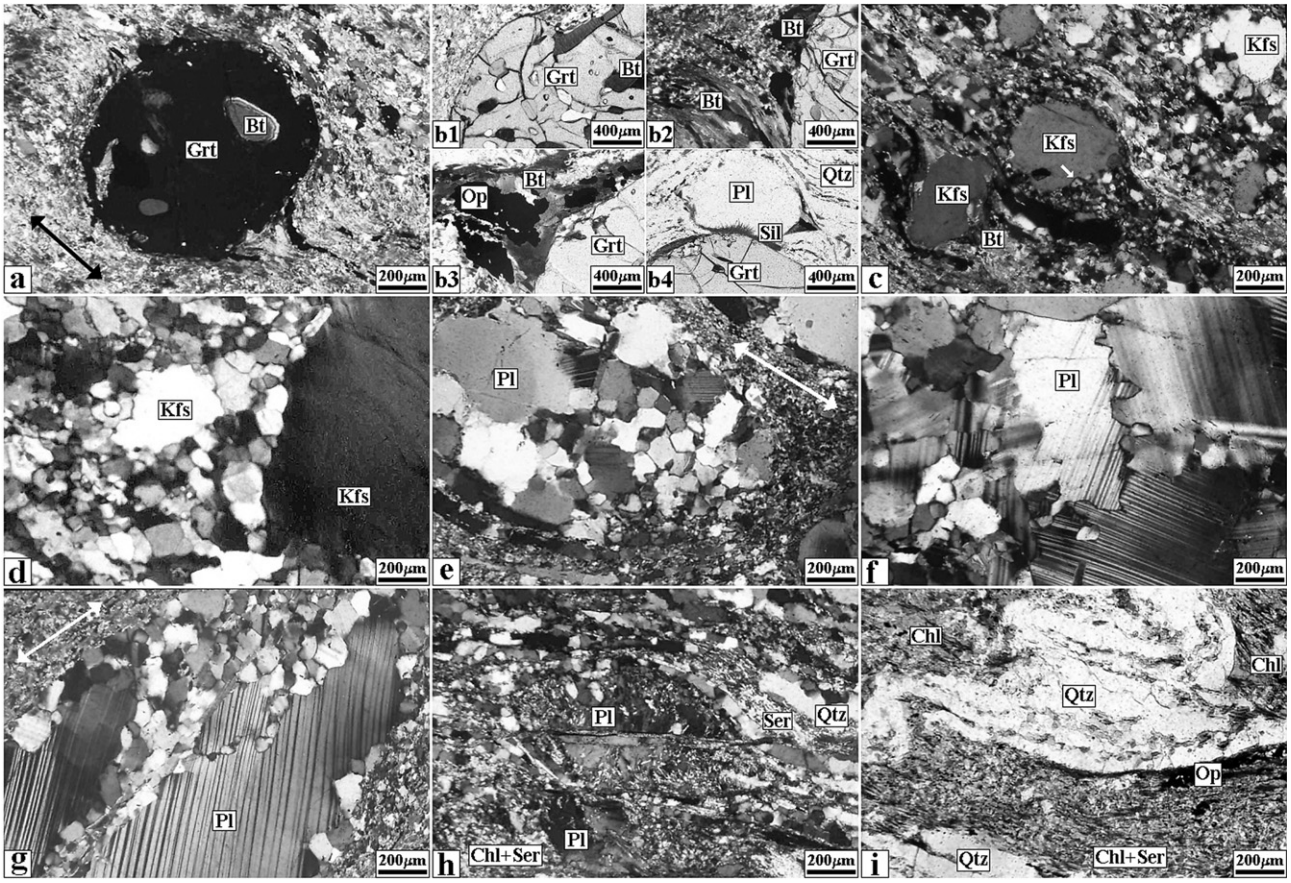

Fig. 4. Photomicrographs of basement mylonites from the central sector of Pringles Metamorphic Complex. Thin section orientation as in Fig. 3. (a) Almost perfectly rounded garnet porphyroclast in a biotite-rich matrix with subordinated recrystallized quartz and feldspars and opaque minerals. Garnet encloses quartz poikilitic inclusions and shows intracrystalline fractures sealed with neoformed biotite. Coarse neoformed biotite and opaque minerals crystallized in porphyroclast pressure shadows. Biotite sealing intracrystalline fractures, crystallized in porphyroclast tails, or forming the fine-grained matrix does not show noticeable compositional differences. Double arrow, mylonitic foliation. Crossed nicols. (b) Several aspects of garnet porphyroclasts; (1) rounded garnet porphyroclast showing intense intracrystalline fracturing and crystallization of coarse strain-free biotite. Each coarse biotite crystal can be linked to one or more fractures sealed with fine-grained biotite and reaching porphyroclast edges; (2 and 3) garnet porphyroclasts with synmylonitic crystallized coarse biotite and opaque minerals at tails; (4) garnet and plagioclase porphyroclasts in contact, example of a strain-induced reaction. This phenomenon is observed between touching feldspar porphyroclasts. In most cases, needle-shaped sillimanite crystals develop at the porphyroclast contacts parallel to the mylonitic foliation (site of high normal stress around the grains). Crystallization of coarse biotite and opaque minerals in plagioclase tails and at low-pressure sites between both porphyroclasts. Plane polarized light. (c) Rounded k-feldspar porphyroclast with serrated edges and recrystallized tails extending parallel to the mylonitic foliation. Virtual lack of intracrystalline deformation and bulging; high-angle boundary to a new grain without visible subgrains (arrow). Bottom right corner, irregularly shaped k-feldspar porphyroclast with ragged boundaries due to replacement by biotite, which constitutes asymmetric tails. Crossed nicols. (d) Recrystallized k-feldspar grains in an extension site developed between two fragments of a big porphyroclast (only right fragment is shown). Coarse polygonal new grains meet at triple junctions, characteristically developed at these sites. Weak intracrystalline deformation in the porphyroclast, high-angle boundaries between the relict and recrystallized grains, absence of subgrains. Some lobated grain boundaries between new grains, evidence of grain boundary mobility. Crossed nicols. (e) Elliptic plagioclase porphyroclast elongated parallel to foliation (double arrow) and intensively recrystallized. Recrystallization advances from the edges and intracrystalline fractures of porphyroclasts. Dissimilar new grain shapes and sizes, grain boundary mobility, and presence of scarce subgrains. Crossed nicols. (f) Detail of plagioclase recrystallization. High grain boundary mobility between relict fragments to bulges limited by high-angle boundaries and localized homogenization of primary twinning. Recrystallized grains tend to develop polygonal with 120° triple junctions. Crossed nicols. (g) Elongated, parallel to foliation plagioclase porphyroclast showing evidence of both GBMR and RR. New grains separated from porphyroclast by high-angle boundaries (without visible subgrains), bulging from intracrystalline microfracture (center), and subgrains with slight deviation of primary twins when passing through a low-angle boundary (center left). Double arrow, mylonitic foliation. Crossed nicols. (h) Mylonitic texture and mineral assemblage overprinted during low-temperature event (T_4). Retrogression occurs along thin bands, at both sides of which the mylonitic texture and paragenesis are unaltered. Thin, continuous microfractures traverse the mylonitic arrangement; intense replacement of feldspars (porphyroclasts and recrystallized grains) by sericite, chlorite, and opaque minerals. Crossed nicols. (i) Another sector (center of band) showing obliteration of the mylonitic texture and intense replacement of mineralogy by lower-temperature assemblage. Remnants of mylonitic texture (folded quartz ribbons) and replacement of the original biotite and feldspars by chlorite and sericite. Plane polarized light. Mineral name abbreviations according to Bucher and Frey (1994).

(Figs. 3i and 4h). Quartz also appears as inclusions in poikilitic garnet, showing only very weak intracrystalline deformation.

Garnet within mylonites shows dissimilar aspects. Most of the original crystals in quartz–feldspar-rich domains preserve irregular shapes and have quartz and plagioclase

as dominant inclusions (Fig. 3h). These garnets have very similar characteristics to those observed in the S/C protomylonites. Garnets located within dark (biotite-rich) domains show the following characteristics: (1) very fractured garnet porphyroclasts with almost perfect circular or slightly elliptical shapes, which usually show abundant biotite sealing intracrystalline fractures (Figs. 3g, h, 4a, b); (2) less commonly, irregularly shaped original garnet grains elongated subparallel to foliation, which are mainly deformed by fracturing subparallel to the flow plane, that show abundant coarse biotite sealing fractures; and (3) small, almost perfectly rounded porphyroclasts, internally less fractured or not fractured and with few or no biotite inclusions, though coarse biotites are commonly observed at their edges and pressure shadows. Some of these small garnets show incipient development of crystalline external faces and incorporation of fine-grained matrix quartz, biotite, and opaque inclusions close to their edges.

Garnets with higher densities of internal fractures are also richer in coarse biotite inclusions. Internal fractures are sealed either with single coarse biotite crystals or aggregates. In most cases, one or more visible microfractures can be related to a given crystal or biotite aggregate (Fig. 4b1). Sometimes, biotite crystals form decussate textures at the intersection of several fractures. Biotites sealing fractures generally show greater sizes than matrix biotites (Figs. 4a, b1). Crystals with comparable sizes are present within the pressure shadows and extension sites between pulled-apart garnet grains (Figs. 4a, b2, and b3) and highly strained feldspar and cordierite porphyroclasts and their tails (Figs. 3f, 4b4, c and e). In all cases, biotite inclusions lack almost all internal deformation. Garnet porphyroclasts and biotite inclusions are optically homogeneous and show equilibrium contacts. Garnet porphyroclasts often contain fine sillimanite needle inclusions, mainly limited to the center of the crystals, and small sillimanite prisms crystallized in extension sites close to the borders of the relict grains. Rounded or elliptic garnet porphyroclasts located within the dark bands are commonly surrounded by asymmetric biotite pressure shadows resembling δ-shaped porphyroclast systems (Fig. 4a).

In the strongly banded mylonites, abundant sillimanite occurs in low-strain domains, usually the light bands. As in protomylonites, both coarse relict and thin neoformed crystals can be recognized. In some cases, the same textural arrangements described for S/C protomylonites are preserved. In sectors dominated by a fine recrystallized matrix (scarce relict grains), remnant coarse sillimanite porphyroclasts usually show sigmoidal mica-fishes shapes. Fine, needle-shaped sillimanite crystal aggregates commonly develop at the mutual contacts between porphyroclasts, as in garnet–feldspar (Fig. 4b4) and feldspar–feldspar pairs. In such cases, sillimanite needles grow at high-angle to the mylonitic foliation and toward the interior of porphyroclasts – a good example of a reaction induced by deformation. In the dark, biotite-bearing bands, sillimanite commonly is restricted to small, needle-shaped crystals within garnet porphyroclasts and, as mentioned previously, to small, euhedral sillimanite grains crystallized in extension sites close to their edges.

Cordierite has been recognized only in the light bands of the mylonites (low-strain domains), where it appears as intensively retrograded porphyroclasts. It is never present as a free phase in the dark bands (high-strain domains), where fine biotite is the essential constituent of the matrix. However, small, altered relics are sometimes preserved as inclusions together with sillimanite and ilmenite in the cores of garnet porphyroclasts.

K-feldspar porphyroclasts are irregular or rounded and show undulatory to patchy extinction and sutured contours due to recrystallization along their boundaries (Fig. 4c). High-angle contacts separate recrystallized grains from porphyroclasts, and subgrains are absent (Figs. 4c and d). Depending on the sample, recrystallized grains can show irregular shapes and sizes of up to 50 μm (e.g., S/C protomylonites) or form aggregates of polygonal crystals, frequently meeting at 120° triple junctions whose sizes range between 150 and 170 μm. Larger, subhedral new grains are mainly developed in porphyroclast borders facing pressure shadows and in intracrystalline fractures (Fig. 4d), whereas in the mylonitic matrix, they usually show smaller grain sizes and irregular shapes (Fig. 4c). Although scarce, some subgrains located close to porphyroclast edges or intracrystalline fractures can be observed. Recrystallized grains often show cross-hatched twinning. In some mylonitic samples, k-feldspar porphyroclasts are absent. However, small, recrystallized grains can be recognized in the matrix, mixed with recrystallized plagioclase grains, neocrystallized biotite, sillimanite needles, and opaque minerals.

Most plagioclase porphyroclasts are rounded or elliptic (Figs. 3g, h, and 4e). No remarkable flattening has been observed, and some relicts of strongly recrystallized original plagioclase porphyroclasts are totally irregular. However, in some mylonitic samples, scarce flattened porphyroclasts (Fig. 4g) coexist with rounded or elliptic porphyroclasts in the same sample. Elliptic porphyroclasts show variable major/minor axis ratios. Major and minor axes often reach 5 and 3 mm, respectively. Porphyroclasts can show undulatory to patchy extinction, bending and homogenization of the primary twins, and secondary twinning (Figs. 4e–g). The contact between relict fragments is commonly serrated due to bulging, which mainly develops from the borders and internal fractures of the strained grains toward the center of the relict portions (Figs. 4e–g). Recrystallized aggregates show unequal grain sizes and dissimilar shapes. Equant new grains reach up to 185 μm, but some elongated grains reach 225 μm for their longest dimension. Although some subhedral new grains tend to develop triple junctions by sectors, most grains are irregular and in contact through lobated grain boundaries. Some flattened porphyroclasts and rounded/elliptic plagioclase grains show patchy extinction due to the presence of kink bands and subgrains delimited by low-angle boundaries (Fig. 4g). Subgrain

rotation is often demonstrated by the continuity of the primary twinning from the relict into the rotated subgrain, though with a slight angular deviation (Fig. 4g). Subgrains of similar sizes as the new grains are located either at the edges of the relict crystals or next to intracrystalline fractures, where aggregates of almost equally sized (up to 200–250 μm) polygonal grains, frequently meeting at 120° triple junctions, can be observed. Small relict fragments entirely surrounded by a recrystallization mantle often show deformation bands, subgrains, and "core and mantle" structures. Sometimes, subgrains and bulging both clearly developed on the same plagioclase crystal (Fig. 4g). In many cases, plagioclase porphyroclasts have been fully recrystallized, forming monomineralic lenses or ribbons developed parallel to foliation. Recrystallized plagioclase crystals always show smaller grain sizes than the surrounding quartz ribbons. Plagioclase porphyroclasts show asymmetric tails (Figs. 3g and h), resembling δ, σ, or complex δ–σ-shaped porphyroclast systems (Passchier and Trouw, 1996). Tails consist mainly of recrystallized plagioclase with scarce k-feldspar recrystallized grains and neocrystallized biotite, opaque minerals, and prismatic sillimanite. These tails do not extend far from the porphyroclasts but often are replaced by the coalescence of two foliation-parallel quartz ribbons.

Small remnants of relict plagioclase crystals surrounded by finer recrystallized plagioclase, k-feldspar grains, and neocrystallized biotite can also be recognized as thin strips or lenticular intercalations within quartz ribbons. Larger plagioclase relicts within these lenses often develop kinematic indicators of the σ-type with fine-grained neocrystallized biotite in the pressure shadows.

Main accessory minerals are zircon and opaque phases. The latter comprise oxides and sulfides and occur in low-pressure sites (porphyroclast pressure shadows and intracrystalline fractures, Figs. 4a and b), as well as disseminated in the matrix, following and enhancing the mylonitic foliation. The amount and size of opaque minerals decrease with distance from the mafic–ultramafic bodies. Sulfides prevail over oxides in mylonites located close to the mafic–ultramafic lenses; this relation is reversed away from the bodies. In basement mylonites immediately adjacent to mafic–ultramafic bodies, the identified sulfides are pyrrhotite, chalcopyrite, and pentlandite. Pyrrhotite with a maximum size of 630 μm is the most abundant sulfide and is partially replaced by chalcopyrite and pentlandite. Ilmenite and magnetite are preferentially located in the matrix, reaching a maximum size of 450 μm along the foliation. Most sulfides and opaque phases show subhedral shapes. Away from the mafic–ultramafic bodies where oxides predominate over sulfides, ilmenite is the most abundant oxide (sometimes with exsolution of hematite), shows subhedral to anhedral shapes, and occurs in low-pressure sites with a maximum size of 500 μm or disseminated in the matrix with sizes of up to 60 μm. Recognized sulfides are pyrrhotite and chalcopyrite; the latter replaces pyrrhotite. They are disseminated in the matrix with sizes usually less than 30 μm but occasionally reach 130 μm in porphyroclast intracrystalline fractures.

5.2. Mafic mylonites

Unlike the surrounding basement country-rocks, where mylonitization is universally distributed and a totally undeformed protolith cannot be identified, the mafic–ultramafic bodies are strongly affected only at their margins and along thin bands (cm to m scale) within the bodies. Mafic mylonites are limited by weakly or almost undeformed coarse-grained rocks, preserving their magmatic mineralogy and texture. Thus, mafic mylonites can be easily correlated with their immediately adjacent protoliths. A mylonitic band (mafic mylonite) developed on a norite (mafic protolith) from Las Águilas River mafic–ultramafic bodies was selected for the analysis.

5.2.1. Mafic protolith

Mesoscopically, the protolith is a dark gray to black, coarse- to medium-grained norite containing orthopyroxene–plagioclase–hornblende–biotite–opaque minerals. Mafic minerals and plagioclase are arranged in a granular texture without any preferred orientation, and the rock shows a rough disjunctive foliation (Twiss and Moores, 1992). Pale-brown biotite shows a tabular {001} habit or pseudo-hexagonal outlines. Small sulfide grains are also mesoscopically recognizable.

Coarse-grained hypidiomorphic-granular norites are optically characterized by texturally equilibrated subhedral orthopyroxene and plagioclase grains (Fig. 5a).

Orthopyroxene crystal sizes are in the range 3–3.5 mm and often show minute clinopyroxene exsolution lamellae. Intracrystalline deformation is shown by slight bending of the exsolution lamellae and patchy extinction due to microfracturing.

Most plagioclase crystals (2–2.5 mm) show intracrystalline deformation, indicated by undulatory to patchy extinctions, bending and homogenization of the primary twinning, deformation bands, and secondary twinning (tapering twins) (Fig. 5a).

Anhedral hornblende grains crystallize in the intergranular spaces between preexisting orthopyroxene and plagioclase crystals. Subhedral hornblende crystal sizes range 1–3 mm. Optically continuous hornblende crystals partially surround or totally enclose fragments of orthopyroxene and plagioclase (Figs. 5b and c). Hornblende also crystallizes in orthopyroxene fractures. This textural characteristic indicates a late magmatic origin for hornblende. Greenish-yellow hornblende crystals show weak internal deformation, as indicated by slight undulatory to patchy extinction. Its almost undeformed character is also demonstrated by the preservation of straight, simple-twin boundaries in some grains.

Biotite grains crystallized interstitially virtually without preferred orientation and show varied shapes, from slightly

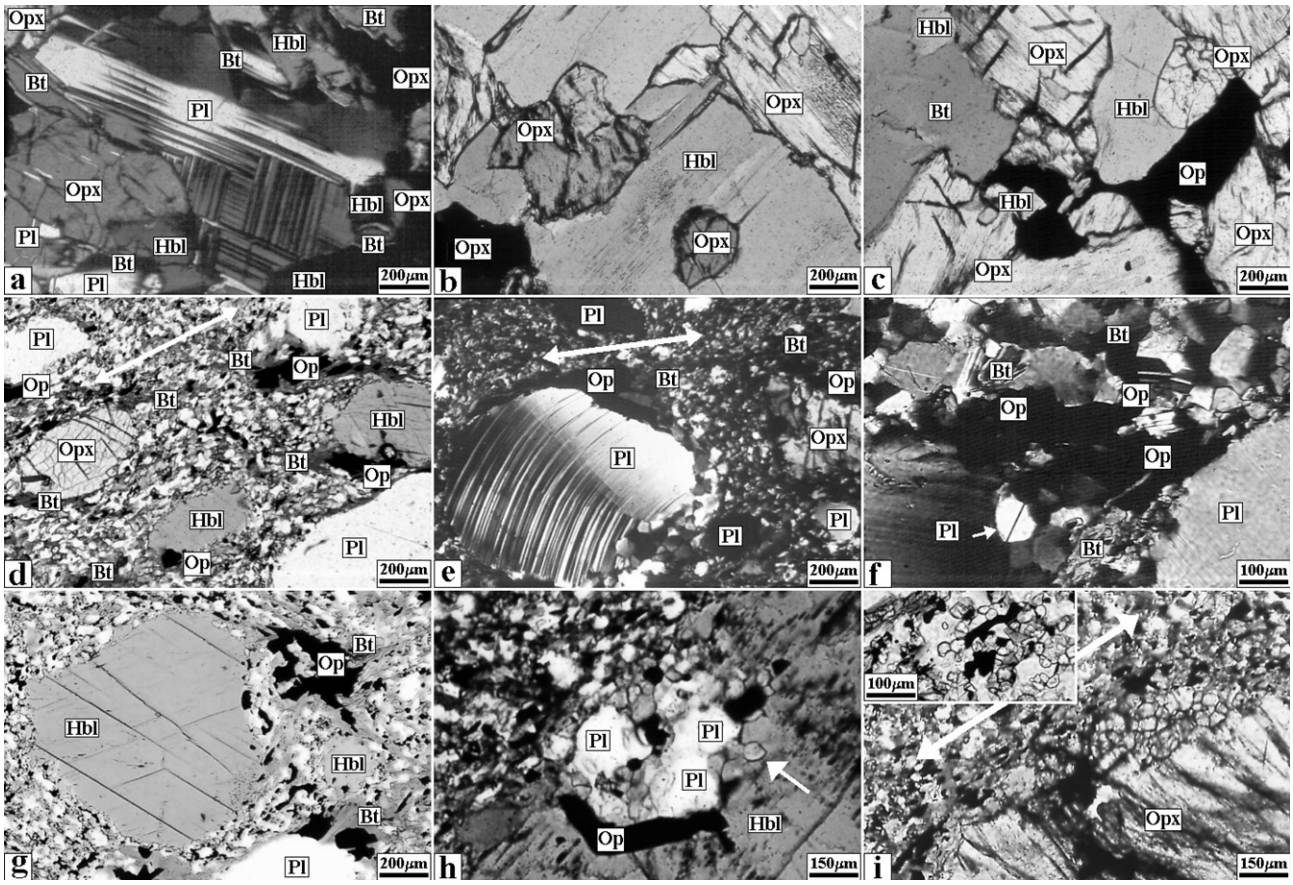

Fig. 5. Photomicrographs of mafic protolith (a–c) and mafic mylonites (d–i) from the central sector of the Pringles Metamorphic Complex. (a) Partially preserved magmatic granular hypidiomorphic texture between orthopyroxene and plagioclase. Moderate intracrystalline deformation evidenced mainly by plagioclase crystals. Orthopyroxene crystals show clinopyroxene exsolution lamellae. Interstitial hornblende and tabular biotite crystals. Crossed nicols. (b) Interstitial hornblende crystal showing optical continuity and enclosing and replacing orthopyroxene grains. Almost total absence of intracrystalline deformation in hornblende; orthopyroxene crystals show undulatory to patchy extinctions and microfractures. Crossed nicols. (c) Interstitial biotite crystal (basal section) and opaque minerals replacing orthopyroxene and hornblende. Plane polarized light. (d) Mafic mylonite showing plagioclase, orthopyroxene, and hornblende porphyroclasts in a matrix composed of recrystallized plagioclase, orthopyroxene, and hornblende grains, neocrystallized biotite, and opaque minerals. Grain sizes in biotite and opaque minerals crystallized in porphyroclast pressure shadows. Double arrow, mylonitic foliation. Plane polarized light. (e) Highly strained plagioclase porphyroclast showing bending and homogenization of primary twinning and intense recrystallization at margins. Rounded plagioclase porphyroclast and bulging, giving way to new grains separated from the relict by high-angle boundaries without visible subgrains. Crystallization of coarse biotite and opaque minerals in the porphyroclast pressure shadow. Double arrow, mylonitic foliation. Crossed nicols. (f) Recrystallized plagioclase new grains showing dissimilar sizes, shapes, and strain intensity. Subhedral grains with straight twins developing triple junctions; other irregular untwinned new grains showing undulatory extinctions. New grains separated from the porphyroclast by high-angle boundary without visible subgrains (arrow). Crystallization of coarse biotite and opaque minerals in the low-pressure site generated between the two plagioclase porphyroclasts located at the bottom left and bottom right corners. Crossed nicols. (g) Hornblende porphyroclasts showing serrated borders and irregular shapes. Lack of strain and filling of the cleavage planes with red-brown biotite. Coarser grain size in the biotite and opaque minerals crystallized in the pressure shadows of hornblende and plagioclase porphyroclasts, opposite the finer grain shown by the same phases disseminated in the matrix. Plane polarized light. (h) Detail of hornblende recrystallization characteristics. Hornblende new grain separated from the porphyroclast through high-angle boundary (arrow) without visible subgrains and arrangements of polygonal new grains (externally intermixed with coarser plagioclase new grains). Greater crystalline size of opaque minerals in the embayment (low-pressure site) in relation to the finer grain developed by opaque minerals in the matrix. Crossed nicols. (i) Detail of orthopyroxene recrystallization characteristics. Polygonal new grains meeting at 120° triple junctions at the border of an orthopyroxene porphyroclast. A detail of the recrystallized orthopyroxene grains disseminated in the matrix in the inset (top right corner). Almost equidimensional orthopyroxene and plagioclase new grains intermixed with neocrystallized biotite and opaque minerals usually elongated parallel to the mylonitic foliation (double arrow). Plane polarized light. Mineral name abbreviations according to Bucher and Frey (1994).

pleochroic basal sections with their contours defined by the intergranular spaces between preexisting minerals (orthopyroxene, plagioclase, hornblende) (Fig. 5c) to highly pleochroic euhedral to subhedral tabular crystals elongated parallel to the {001} cleavage (Fig. 5a). Tabular crystals are up to 1.5 mm long. Biotite crystals are inhomogeneously distributed in the rock, practically absent in some sectors and very abundant in others. Biotites do not show evidence of intracrystalline deformation and occasionally partially replace hornblende crystals (Fig. 5c).

Opaque minerals (sizes up to 0.7 mm) crystallized interstitially and are inhomogeneously distributed in the rock. The opaque phases are more abundant in the biotite-rich portions. Some opaque phases fill fractures within

orthopyroxenes (Fig. 5c). The dominant opaque minerals are pyrrhotite, chalcopyrite, pentlandite, pyrite, and ilmenite. The modal amount does not exceed 1%. These minerals are located along the contacts between silicate grains, cleavage planes, and intragranular microfractures. Pyrrhotite is the most abundant sulfide, which occurs as anhedral and subhedral grains up to 0.72 mm in size, and carries pentlandite "flame-like" exsolutions. Chalcopyrite crystals are scarce in this rock and most often occur associated with pyrrhotite crystals; the grains have anhedral shapes and a maximum size of approximately 0.17 mm. Pentlandite is present as flame-like exsolutions and very thin veins in pyrrhotite. Only scarce anhedral grains of pyrite have been identified. Ilmenite is the only identified oxide phase, which occurs as anhedral crystals not exceeding 0.02 mm.

5.2.2. Mafic mylonites

Mesoscopically, these rocks are moderately to intensely foliated, dark to almost black porphyroclastic mylonites. Pyroxene, hornblende, plagioclase, and garnet porphyroclasts show variable sizes and shapes. Very small sulfide grains (<0.1 mm) and biotite laths are abundant, mainly distributed along mylonitic foliation planes.

Microscopically, mafic mylonites display a porphyroclastic microstructure (porphyroclasts constitute approximately 40% of the sample) and are composed of plagioclase, hornblende, orthopyroxene, and garnet porphyroclasts, surrounded by a fine-grained matrix of recrystallized (orthopyroxene–plagioclase–hornblende) and neocrystallized (biotite–opaque minerals) phases (Fig. 5d). The mineralogy and texture of the adjacent protolith is partially preserved in scarce polyphasic microlithons.

Plagioclase porphyroclasts are mainly rounded to elliptic in shape (Figs. 5d and e), though some irregular clasts can be observed at sizes of up to 2 mm. The porphyroclasts display undulatory extinction, bending, partial homogenization of the primary twinning in highly strained crystalline sectors, secondary twinning (tapering twins or cross-hatched twinning), and intense recrystallization (Figs. 5e and f). Recrystallization occurs at porphyroclast borders, in intracrystalline fractures between separated fragments of boudinaged grains, and in pressure shadows. New grains have dissimilar grain sizes (20–110 μm), most in the range 50–60 μm. Recrystallization gives rise to the local formation of polygonal grain aggregates meeting at 120° triple junctions (Figs. 5e and f). Some recrystallized grains are euhedral to subhedral and show straight twinning and uniform extinction, whereas irregular and smaller grains show undulatory extinction (Fig. 5f).

Hornblende porphyroclasts, with a maximum size of 2.5 mm, exhibit elliptic or irregular shapes and serrated borders (Figs. 5d–g). The intracrystalline deformation of porphyroclasts is hardly noticeable except for the weak undulatory extinction shown by some crystals. Evidence of recrystallization can be recognized in some porphyroclasts by the presence of bulges and formation of polygonal new grains, separated from the relictic ones by high-angle boundaries (Fig. 5h). Aggregates of polygonal new grains, joining at triple junctions, can be recognized close to porphyroclasts. However, the most common situation is that of new grains rapidly forming a fine polyphase intermix with other matrix constituents (Figs. 5d–g). Grain sizes in the matrix vary between 30 and 80 μm. Hornblende porphyroclasts often show neominerals, such as biotite and opaque phases at their margins, cleavage planes, microfractures, and pressure shadows (Figs. 5d, g and h).

Orthopyroxene porphyroclasts (Fig. 5d) are irregular in shape and of variable sizes, reaching 3–3.5 mm. The intracrystalline deformation is indicated by weak undulatory extinction and fracturing. Some crystals are bent, as indicated by slightly curved exsolved clinopyroxene laths. Recrystallization occurs at the margins of some porphyroclasts, where aggregates of almost perfect polygonal crystals of up to 80–90 μm in size and meeting at 120° triple junctions can be observed (Fig. 5i). Subhedral recrystallized matrix grains often range in size between 15 and 50 μm (Fig. 5i, inset).

Garnet porphyroclasts have textural characteristics similar to those observed in the mylonites developed in the gneissic–migmatitic country rocks. Elliptic or irregular porphyroclasts, up to 4–4.5 mm long, have plagioclase inclusions, which indicate their original poikiloblastic growth. This characteristic represents the unique difference with garnet crystals of the country rocks, in which quartz is the dominant inclusion with subordinate plagioclase. As in the country rocks, porphyroclasts show a high density of internal fractures filled with biotite and opaque phases. These phases are also abundant in the pressure shadows of the porphyroclasts. In these low-pressure sites and in internal fractures, biotites and opaque phases virtually lack intracrystalline deformation and develop grains with greater sizes than the same phase disseminated in the matrix. Small satellite garnets (0.5 mm) with irregular shapes are often associated with big porphyroclasts. Separated from the porphyroclasts, they develop crystalline faces and enclose abundant amounts of fine-grained biotite and opaque inclusions from the matrix.

Some sectors of the matrix show a predominance of recrystallized grains (plagioclase, hornblende, orthopyroxene), whereas in other areas, these phases are intermixed with abundant neoformed biotite and opaque minerals. Recrystallized plagioclase grains usually have greater sizes (up to 110 μm) than hornblende (80 μm) and orthopyroxene (50 μm) new grains (Figs. 5d–i, inset). These recrystallized phases are more or less equidimensional, whereas fine-grained biotites (150 μm) and opaque minerals usually develop elongated grains, with their longest dimension parallel to the mylonitic foliation (Fig. 5i, inset). Although opaque phases are abundant in the rock as a whole, they seem to be spatially linked to biotite (in both modal proportion and crystal size). The neoformed biotite and opaque grains have greater sizes when they fill internal porphyroclast fractures or are crystallized in low-pressure sites (e.g., porphyroclasts embayments, extension fractures,

between boudinaged grain fragments, pressure shadows, Figs. 5d–i). In these sites, tabular biotite crystals reach 0.5–0.6 mm in length.

Sulfides and oxides (10–12 modal% of the sample) are disseminated in the matrix with a maximum size of 30 μm and oriented parallel to rock foliation. They also occur in fractures affecting porphyroclasts and in low-pressure sites, where they usually develop greater grain sizes. Pyrrhotite is the most abundant sulfide and occurs as anhedral to subhedral grains that do not exceed 100 μm. Generally, it is located in extension sites between porphyroclasts. Pentlandite occurs as crystals and in the form of flame-like exsolutions, always associated with pyrrhotite. Chalcopyrite crystals do not exceed 80 μm and display anhedral shapes. This mineral frequently occurs associated with pyrrhotite, with textural evidence indicating that chalcopyrite replaces it. Anhedral pyrite crystals not exceeding 60 μm are associated with pyrrhotite and chalcopyrite, in the latter case replacing it. Both magnetite and ilmenite (average maximum sizes of 30 μm) are present in the mylonitic matrix. Magnetite is the most abundant oxide phase and usually replaces sulfides. Some sulfide clusters (pirrhotite–chalcopyrite–pyrite) are surrounded by biotite crystals.

6. Geothermobarometry

The TWEEQU program (Berman, 1991) – with thermodynamic data of Berman (1988) updated in March 1997 (version 2.02 b) with internally consistent solid solution and end-member data for (1) garnet, olivine, orthopyroxene, cordierite, and ilmenite from Berman and Aranovich (1996); (2) clinopyroxene (Berman et al., 1995); and (3) biotite and Mg–Fe spinel based on Berman and Aranovich (unpublished data) – was used to evaluate the physical conditions of the mylonitic event.

Six representative mylonites from different localities within the studied shear zone were selected. Five belong to the mylonitized gneissic–migmatitic basement (a protomylonite and four mylonites) and the other to a mafic mylonite adjacent to mafic–ultramafic bodies.

Microprobe chemical analyses of selected relict, recrystallized, and neocrystallized minerals were performed to test the phases for internal zonation. Because garnet frequently develops zonation in response to changes in the physical conditions of metamorphism, we performed detailed profiles on several porphyroclasts of different basement mylonitic samples. These profiles show that garnets are compositionally homogeneous (Figs. 6a and b), a common characteristic of garnet subjected to very high-grade metamorphic conditions (upper amphibolite to granulite facies) due to the rapid diffusion of elements at very high temperatures (e.g., Yardley, 1989; Spear, 1995). These extreme conditions usually eliminate all evidence of zonation developed during progressive metamorphism. However, the garnet in Fig. 6c shows a very slight increase of manganese and calcium and a clear increase of Fe# in a zone located less than 50 μm from the porphyroclast border. A commonly observed characteristic in the studied samples is a Fe# increase in garnet and decrease in biotite at the borders of crystals in mutual contact. This characteristic disappears away from the mutual contact, and both minerals become homogeneous. This behavior is expected for garnet–biotite pairs undergoing an exchange reaction of the type almandine + phlogopite ⇆ pyrope + annite; it enables them to maintain partitioning equilibrium with decreasing temperatures (e.g., Spear, 1995). The compositional garnet profile in Fig. 6c ends on both extremes at contacts with biotite crystals, whereas garnet profiles in Figs. 6a and b end at contacts with other phases. Thus, the apparent zonation shown by garnet in Fig. 6c is not a real zonation but the result of a subsequent reequilibration by the interchange of elements through diffusion at the borders between garnet and biotite in mutual contact, during cooling following the mylonitic event.

Like garnet porphyroclasts, relict and recrystallized plagioclase grains are homogeneous. Plagioclase recrystallized grains may show small differences in composition with respect to porphyroclasts, usually a weak increase in Na_2O and K_2O.

Except for cordierite in basement mylonites, which appears intensely retrogressed, the rest of the minerals are fresh and not zoned.

These characteristics indicate that all phases in each of the samples equilibrated during the mylonitization event, and only local mineral chemical variations exist due to exchange reactions between suitable phases (e.g., garnet–biotite) during the cooling period that followed the mylonitic event. Reequilibration is also clearly shown by mafic mylonites, for which the parental relationship with protoliths is demonstrated by their common modal composition and field relationships. The chemical composition of relict phases in mafic mylonites (porphyroclasts) has been entirely reequilibrated to mylonitization conditions (e.g., orthopyroxene–plagioclase–hornblende of M67-SL versus M68-SL, Tables 1 and 2). As with the basement mylonites, no mineral chemical zonations are observed in mafic mylonites.

For all basement mylonites, the following mineral association was used for the TWEEQU calculation: garnet + biotite + sillimanite + k-feldspar + plagioclase + quartz + fluid (H_2O–CO_2) in the KCFMAS-HC system. P–T and T–XCO_2 calculated diagrams for one of the basement mylonites (M3-SL) appear as an example in Fig. 7. The rest of the samples gave equivalent degrees of fitting in the calculated reactions. P–T–XCO_2 determined for the five basement mylonites based on eight reactions (three independent) (lower left side of Fig. 7), with the same system and assemblage, appear on the lower right-hand side of the figure. The mineral compositions used for the calculations are presented in Tables 1 and 2. A comparison of the five samples shows slight dispersion in the pressure values (6.28–6.85 kbar) and a greater scatter in the temperatures (687-762 °C).

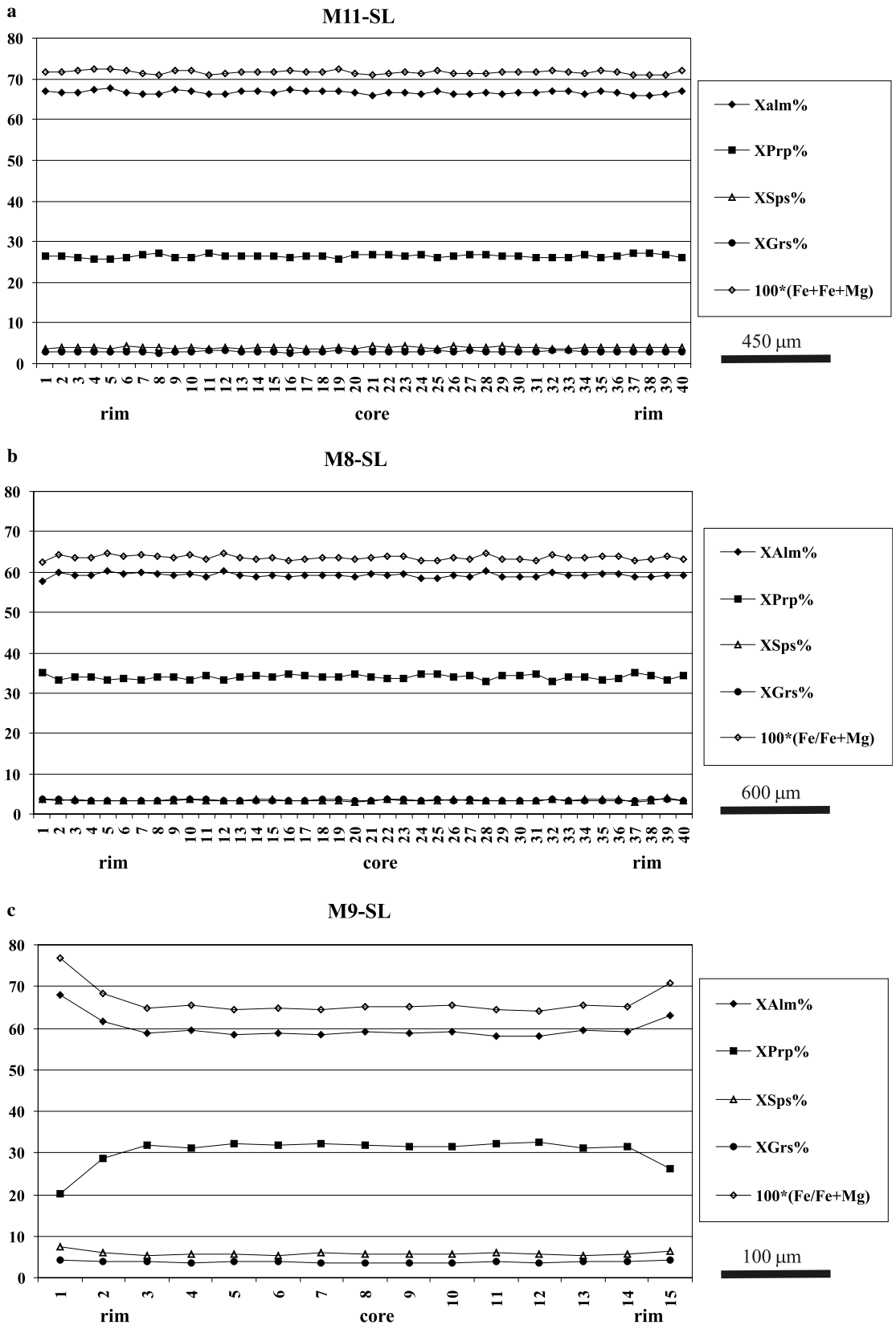

Fig. 6. Microprobe traverses on garnets from basement mylonites. Lack of chemical zonation in samples M11-SL and M8-SL. Apparent zonation in sample M9-SL is due to local Fe/Mg exchange reaction, implying biotite crystals at both extremes of the profile. No calcium zonation, as occurs in homogeneous garnets.

Table 1
Representative electron microprobe analysis of garnets, biotites, hornblendes, and orthopyroxenes

Garnets							Biotites								Hornblendes			Orthopyroxenes		
Sample	M3-SL	M7-SL	M9-SL	M11-SL	M14-SL	M67-SL	Sample	M3-SL	M7-SL	M9-SL	M11-SL	M14-SL	M67-SL	M68-SL	Sample	M67-SL	M68-SL	Sample	M67-SL	M68-SL
SiO_2	38.13	38.24	37.14	38.23	37.41	38.48	SiO_2	36.35	35.46	35.55	35.74	35.24	37.10	38.49	SiO_2	46.84	47.82	SiO_2	53.04	54.56
TiO_2	0.05	0.01	0.06	0.04	0.02	0.04	TiO_2	4.81	3.16	2.70	4.47	4.09	3.40	3.3	TiO_2	1.26	0.98	TiO_2	0.06	0.05
Al_2O_3	20.99	21.09	21.34	21.02	21.05	21.73	$A1_2O_3$	16.59	17.76	17.64	16.5	16.72	16.45	16.08	$A1_2O_3$	9.73	9.97	$A1_2O_3$	1.45	1.60
FeO	29.99	32.93	29.85	31.42	33.51	27.07	FeO	14.15	16.50	13.75	16.27	16.21	14.15	7.55	FeO	10.99	6.79	FeO	21.38	14.56
MnO	1.18	1.24	2.88	1.86	1.48	1.61	MnO	0.06	0.02	0.07	0.03	0.05	0.03	0.03	MnO	0.20	0.12	MnO	0.57	0.32
MgO	6.62	4.48	5.90	6.16	4.44	6.57	MgO	12.76	10.51	12.25	11.2	10.44	14.83	19.73	MgO	14.82	17.45	MgO	22.05	28.53
CaO	1.30	2.21	1.50	1.19	1.53	4.88	CaO	0.02	0.00	0.04	0.02	0.03	0.21	0.05	CaO	11.38	11.73	CaO	0.35	0.23
Na_2O	0.16	0.00	0.02	0.02	0.03	0.02	Na_2O	0.23	0.17	0.16	0.16	0.11	0.27	0.46	Na_2O	1.17	1.26	Na_2O	0.03	0.01
K_2O	0.02	0.02	0.02	0.04	0.02	0.00	K_2O	9.68	9.96	9.29	9.93	9.81	8.90	8.89	K_2O	0.53	0.42	K_2O	0.02	0.01
Cr_2O_3	0.05	0.00	0.04	0.00	0.00	0.04	Cr_2O_3	0.09	0.00	0.06	0.02	0.00	0.06	0.66	Cr_2O_3	0.15	0.73	Cr_2O_3	0.03	0.15
Total	98.49	100.22	98.74	99.98	99.50	100.44	Total	94.74	93.54	91.51	94.34	92.70	95.40	95.24	Total	97.07	97.27	Total	98.98	100.02
Number of ions on the basis of 12 Ox. and 8 Cat.							Number of ions on the basis of 22 Ox.								Number of ions on the basis of 23 Ox			Number of ions on the basis of 6 Ox. and 4 Cat.		
Si	3.033	3.040	2.967	3.022	3.000	2.983	Si	5.451	5.452	5.490	5.451	5.467	5.243	5.280	Si	6.763	6.762	Si	1.992	1.951
Al	0.000	0.000	0.033	0.000	0.000	0.017	Al	2.549	2.548	2.510	2.549	2.533	2.738	2.598	Al	1.237	1.238	Al	0.008	0.049
Sum	3.033	3.040	3.000	3.022	3.000	3.000	Sum	8.000	8.000	8.000	8.000	8.000	7.981	7.878	Fe^{3+}	0.000	0.000	Fe^{3+}	0.000	0.000
															Ti	0.000	0.000	Sum T	2.000	2.000
Al	1.967	1.975	1.976	1.957	1.989	1.966	Al	0.381	0.668	0.698	0.415	0.521	0.000	0.000	Sum T	8.000	8.000			
Fe^{3+}	0.000	0.000	0.000	0.000	0.000	0.000	Ti	0.543	0.365	0.314	0.513	0.477	0.361	0.341				Al	0.056	0.018
Ti	0.003	0.001	0.004	0.002	0.001	0.002	Cr	0.011	0.000	0.007	0.002	0.000	0.007	0.071	Al	0.417	0.423	Ti	0.002	0.001
Cr	0.003	0.000	0.003	0.000	0.000	0.002	Fe_t	1.770	2.120	1.780	2.080	2.100	1.672	0.866	Cr	0.017	0.082	Fe^{3+}	0.000	0.025
Sum	1.973	1.975	1.983	1.959	1.990	1.971	Mg	2.853	2.409	2.820	2.547	2.414	3.124	4.035	Fe^{3+}	0.375	0.352	Fe^{2+}	0.000	0.000
							Mn	0.008	0.003	0.009	0.004	0.007	0.004	0.003	Ti	0.137	0.104	Cr	0.001	0.004
Fe^{2+}	1.994	2.182	1.987	2.064	2.240	1.756	Sum	5.566	5.565	5.628	5.561	5.519	5.168	5.316	Mg	3.190	3.679	Mg	0.941	0.952
Mg	0.785	0.531	0.703	0.726	0.532	0.759									Fe^{2+}	0.852	0.354	Sum M1	1.000	1.000
Mn	0.080	0.084	0.196	0.125	0.101	0.106	Ca	0.003	0.000	0.007	0.003	0.005	0.032	0.007	Mn	0.012	0.007			
Ca	0.111	0.188	0.128	0.101	0.130	0.405	Na	0.067	0.051	0.048	0.047	0.033	0.074	0.122	Ca	0.000	0.000	Mg	0.294	0.569
Na	0.025	0.000	0.003	0.003	0.006	0.003	K	1.852	1.954	1.830	1.932	1.941	1.605	1.556	Sum C	5.000	5.000	Fe^{2+}	0.671	0.411
Sum	2.994	2.984	3.017	3.018	3.009	3.029	Sum	1.922	2.005	1.885	1.982	1.979	1.711	1.685				Mn	0.018	0.010
															Mg	0.000	0.000	Ca	0.014	0.009
Mg#	0.28	0.20	0.26	0.26	0.19	0.30	End-members (mol %)								Fe^{2+}	0.100	0.097	Na	0.002	0.001
															Mn	0.012	0.007	K	0.001	0.000
End-members (mol %)							Ann	38.29	46.81	38.70	44.95	46.52	34.86	17.67	Ca	1.760	1.777	Sum M2	1.000	1.000
							Phl	61.71	53.19	61.30	55.05	53.48	65.14	82.33	Na	0.127	0.118			
Alm	66.60	73.12	65.86	68.39	74.44	57.97									Sum B	2.000	2.000			
Adr	0.00	0.00	0.00	0.00	0.00	0.00												End-members (mol %)		
Grs	3.56	6.30	4.09	3.35	4.32	13.27									Ca	0.000	0.000			
Prp	26.22	17.79	23.30	24.06	17.68	25.06									Na	0.200	0.227	Wo	0.73	0.45
Sps	2.67	2.82	6.50	4.14	3.36	3.50									K	0.098	0.076	En	63.69	77.01
Uv	0.15	0.00	0.15	0.00	0.00	0.10									Sum A	0.298	0.303	Fs	35.58	22.54

M3-SL, basement protomylonite; M7-SL, M9-SL, M11-SL, and M14-SL, basement mylonites; M67-SL, mafic mylonite; M68-SL, mafic protolith. Fe^{2+}/Fe^{3+} calculated stequiometrically.

Table 2
Representative electron microprobe analysis of plagioclases, K-feldspars, sillimanites, and ilmenites

Plagioclases								K-feldspars					Sillimanites			Ilmenites		
Sample	M3-SL	M7-SL	M9-SL	M11-SL	M 14-SL	M67-SL	M68-SL	M3-SL	M7-SL	M9-SL	M11-SL	M 14-SL	Sample	M3-SL	M11-SL	Sample	M3-SL	M15-SL
SiO_2	59.92	56.97	56.79	60.87	60.46	47.23	46.94	64.03	64.39	63.19	63.44	63.23	SiO_2	37.37	37.76	SiO_2	0.47	0.36
TiO_2	0.02	0.04	0.05	0.03	0.00	0.04	0.01	0.18	0.23	0.29	0.27	0.15	TiO_2	0.06	0.00	TiO_2	52.88	52.46
Al_2O_3	24.99	27.32	25.49	23.91	24.89	33.40	33.45	18.32	18.42	17.95	17.93	18.04	Al_2O_3	61.41	61.42	Al_2O_3	0.24	0.12
FeO	0.05	0.15	0.11	0.10	0.23	0.28	0.09	0.1	0.16	0.06	0.02	0.20	FeO	0.22	0.71	FeO	41.86	40.78
MnO	0.04	0.04	0.00	0.03	0.01	0.01	0.02	0.02	0.00	0.00	0.03	0.02	MnO	0.01	0.00	MnO	0.26	4.15
MgO	0.00	0.00	1.24	0.00	0.72	0.15	0.08	0.15	0.00	0.00	0.06	0.71	MgO	0.04	0.00	MgO	0.88	1.73
CaO	6.90	9.28	7.63	6.06	6.14	16.74	17.29	0.06	0.00	0.06	0.10	0.03	CaO	0.03	0.02	CaO	0.03	0.08
Na_2O	7.43	5.81	7.58	7.83	8.09	2.05	1.93	1.12	0.54	0.86	0.96	1.09	Na_2O	0.06	0.06	Na_2O	0.21	0.00
K_2O	0.14	0.20	0.12	0.19	0.11	0.13	0.02	14.9	15.68	15.24	15.33	15.13	K_2O	0.02	0.00	K_2O	0.08	0.01
Cr_2O_3	0.00	0.00	0.03	0.01	0.00	0.00	0.00	0.03	0.00	0.01	0.00	0.00	Cr_2O_3	0.05	0.03	Cr_2O_3	0.06	0.22
Total	99.49	99.81	99.04	99.03	100.65	100.03	99.83	98.91	99.42	97.66	98.14	98.60	Total	99.26	100.00	Total	96.97	99.79
Number of ions on the basis of 8 Ox. and 5 Cat.													Number of ions on the basis of 20 Ox. and 12 Cat.			Number of ions on the basis of 6 Ox. and 4 Cat.		
Si	2.681	2.558	2.576	2.730	2.676	2.171	2.162	2.983	2.989	2.987	2.986	2.966	Si	4.067	4.085	Si	0.024	0.018
Al	1.317	1.445	1.362	1.263	1.297	1.808	1.815	1.005	1.007	0.999	0.994	0.996	Ti	0.005	0.000	Ti	2.050	1.962
Fe^{3+}	0.000	0.000	0.000	0.000	0.000	0.000	0.000	0.000	0.000	0.000	0.000	0.000	Al	7.877	7.833	Al	0.015	0.007
Ti	0.001	0.001	0.002	0.001	0.000	0.001	0.000	0.006	0.008	0.010	0.010	0.005	Fe^{3+}	0.000	0.007	Fe^{3+}	0.000	0.024
Fe^{2+}	0.002	0.006	0.004	0.004	0.009	0.011	0.003	0.004	0.006	0.002	0.001	0.008	Fe^{2+}	0.020	0.057	Fe^{2+}	1.804	1.672
Mn	0.002	0.002	0.000	0.001	0.000	0.000	0.001	0.001	0.000	0.000	0.001	0.001	Mn	0.000	0.000	Mn	0.011	0.175
Mg	0.000	0.000	0.084	0.000	0.048	0.010	0.005	0.010	0.000	0.000	0.004	0.050	Mg	0.007	0.000	Mg	0.068	0.128
Ca	0.331	0.446	0.371	0.291	0.291	0.824	0.853	0.003	0.000	0.003	0.005	0.002	Ca	0.004	0.002	Ca	0.002	0.004
Na	0.645	0.506	0.667	0.681	0.694	0.183	0.172	0.101	0.049	0.079	0.088	0.099	Na	0.013	0.013	Na	0.021	0.000
K	0.008	0.011	0.007	0.011	0.006	0.008	0.001	0.885	0.928	0.919	0.921	0.905	K	0.003	0.000	K	0.005	0.001
Sum	4.987	4.975	5.073	4.982	5.021	5.016	5.012	4.998	4.987	4.999	5.010	5.032	Cr	0.004	0.003	Cr	0.000	0.009
													Sum	12.000	12.000	Sum	4.000	4.000
End-members (mol %)																		
Ab	65.50	52.50	63.80	69.30	70.00	18.00	16.80	10.20	5.00	7.90	8.70	9.80						
An	33.60	46.30	35.50	29.60	29.40	81.20	83.10	0.30	0.00	0.30	0.50	0.20						
Or	0.80	1.10	0.70	1.10	0.60	0.80	0.10	89.50	95.00	91.80	90.80	90.00						

M3-SL, basement protomylonite; M7-SL, M9-SL, M11-SL, M14-SL, and M15-SL, basement mylonites; M67-SL, mafic mylonite; M68-SL, mafic protolith. Fe^{2+}/Fe^{3+} calculated stequiometrically.

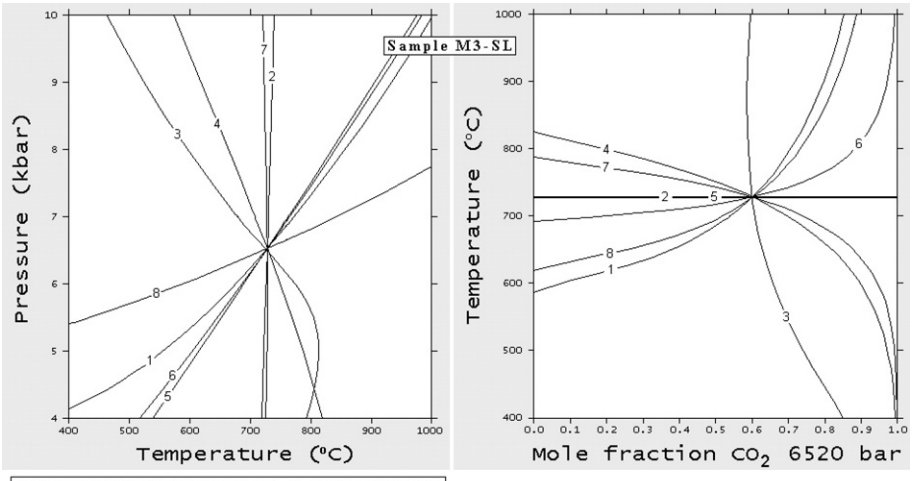

SYSTEM: KCMFSAH; PHASES: Grt-Bt-Sil-Pl-Kfs-Qtz-F(H_2O-CO_2)
REACTION LIST
1) 3 Qtz + 3 An + 2 Ann = 2 Alm + Grs + 2 Kfs + 2 H_2O
2) Ann + Prp = Phl + Alm
3) Kfs + Alm + H_2O = Ann + 2 Qtz + Sil
4) Grs + 2 Kfs + 2 Prp + 2 H_2O = 3 Qtz + 2 Phl + 3 An
5) 3 An = 2 Sil + Qtz + Grs
6) Ann + 6 An = 3 Sil + Kfs + 2 Grs + Alm + H_2O
7) Kfs + Prp + H_2O = Sil + 2 Qtz + Phl
8) 6 An + Phl = 3 Sil + Prp + Kfs + 2 Grs + H_2O

Sample	M3-SL	M7-SL	M9-SL	M11-SL	M14-SL
T (°C)	728	713	709	762	687
P (Kb)	6.52	6.85	6.28	6.85	6.59
XCO_2	0.60	0.54	0.72	0.29	0.54

Fig. 7. *P–T–X*CO_2 conditions for the mylonitic event determined with sample M3-SL (basement protomylonite). Equivalent fitting of the same curves on *P–T–X*CO_2 diagrams, obtained with samples M7-SL, M9-SL, M11-SL, and M14-SL (basement mylonites), using same chemical system and phase association. List of calculated reactions (three independent) and mineral compositions used shown at base.

For the mafic mylonite adjacent to mafic–ultramafic bodies, the following association was used: garnet + biotite + orthopyroxene + plagioclase + quartz + k-feldspar + fluid (H_2O–CO_2). K-feldpar is not observed in these mylonites, but the abundant crystallization of biotite requires a potassium phase or the supply of this chemical component during the mylonitization event. The presence of garnet (absent in the adjacent mafic protolith) indicates that the mylonitic band developed on or close to the contact between the mafic body and the migmatitic country-rocks. Thus, k-feldspar (similar to garnet) could have been present as a solid phase as a result of the interaction between mafic bodies and migmatitic country-rocks before mylonitization, or potassium may have been incorporated in

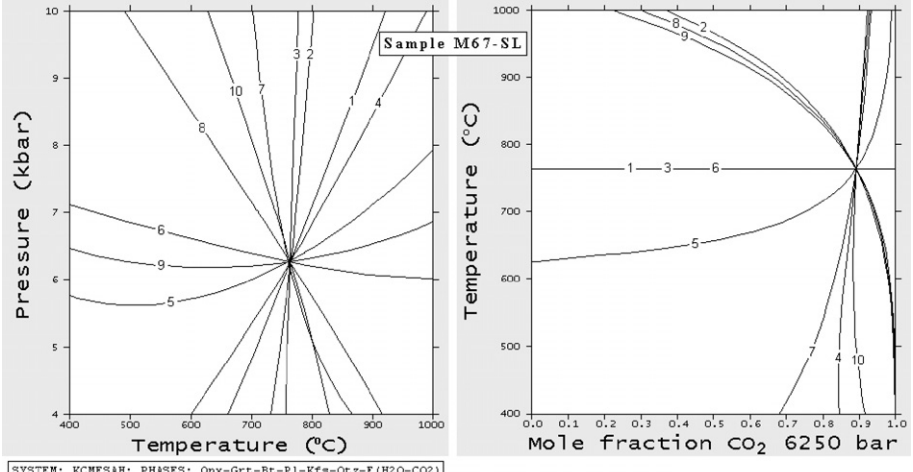

SYSTEM: KCMFSAH; PHASES: Opx-Grt-Bt-Pl-Kfs-Qtz-F(H2O-CO2)
REACTION LIST
1) 2 Alm + Grs + 2 Phl + 3 Qtz = 6 En + 3 An + 2 Ann
2) Phl + 3 Qz = Kfs + 3 En + H_2O
3) Phl + Alm = Ann + Prp
4) Prp + Phl + Grs + 2 Alm + H_2O = 2 Ann + 3 An + 3 En
5) 2 Kfs + Grs + 2 Alm + 2 H_2O = 2 Ann + 3 An + 3 Qtz
6) Grs + 2 Prp + 3 Qtz = 6 En + 3 An
7) Ann + Prp + 3 Qtz = Kfs + 3 En + Alm + H_2O
8) 2 Prp + Kfs + Grs + H_2O = 3 An + 3 En + Phl
9) Prp + Kfs + Grs + Alm + H_2O = Ann + 3 An + 3 En
10) Grs + 2 Kfs + 2 Frp + 2 H_2O = 3 Qtz + 2 Phl + 3 An

Sample	M67-SL
T (°C)	764
P (Kb)	6.25
XCO_2	0.89

Fig. 8. *P–T* and *T–X*CO_2 diagrams showing the conditions of mylonitization for the mafic mylonite (M67-SL). List of calculated reactions (three independent) and mineral compositions used shown at base.

solution from the k-feldspar–bearing adjacent migmatitic country-rocks during mylonitization. Because k-feldspar is a pure end-member, its incorporation into the calculation does not affect the thermobarometric results, which are governed mainly by the exchange reaction [3] (Grt-Bt geothermometer) and the net-transfer reaction [6] (GAES geobarometer). P–T and T–$X\mathrm{CO}_2$ calculated diagrams for the system KCMFAS-HC appear in Fig. 8, and we provide the mineral compositions used in the calculation in Tables 1 and 2. Pressure and temperature results (6.3 kbar, 764 °C) based on ten reactions (three independent) (lower left side of Fig. 8), agree with the P–T conditions obtained for the basement mylonites.

7. Petrogenetic grid

The P–T conditions obtained through thermobarometry can be verified by constructing a suitable petrogenetic grid that constrains the stability field of the phase associations equilibrated during the mylonitic event. We created a phase diagram corresponding to the basement rocks adjacent to mafic–ultramafic bodies with the updated version (2003) of the PERPLEX program (Connolly and Kerrick, 1987; Connolly, 1990) and the database of Holland and Powell (1998). On the basis of petrographic observations, the following phases were considered for the system TKFMAS-HC: cordierite–orthopyroxene–biotite–k-feldspar–sillimanite–quartz–muscovite– rutile–ilmenite-fluid ($H_2O + CO_2$).

The stability of the association k-feldspar + sillimanite and the total absence of muscovite/sericite indicate that the reaction muscovite + quartz ⇆ k-feldspar + sillimanite + H_2O (Fig. 9) defines the minimum temperature conditions for the mylonitic deformation. This reaction, usually called the second sillimanite isograd, requires temperatures in excess of 660 °C at the calculated pressures (6.3–6.9 kbar; rectangle in Fig. 9). However, petrographic

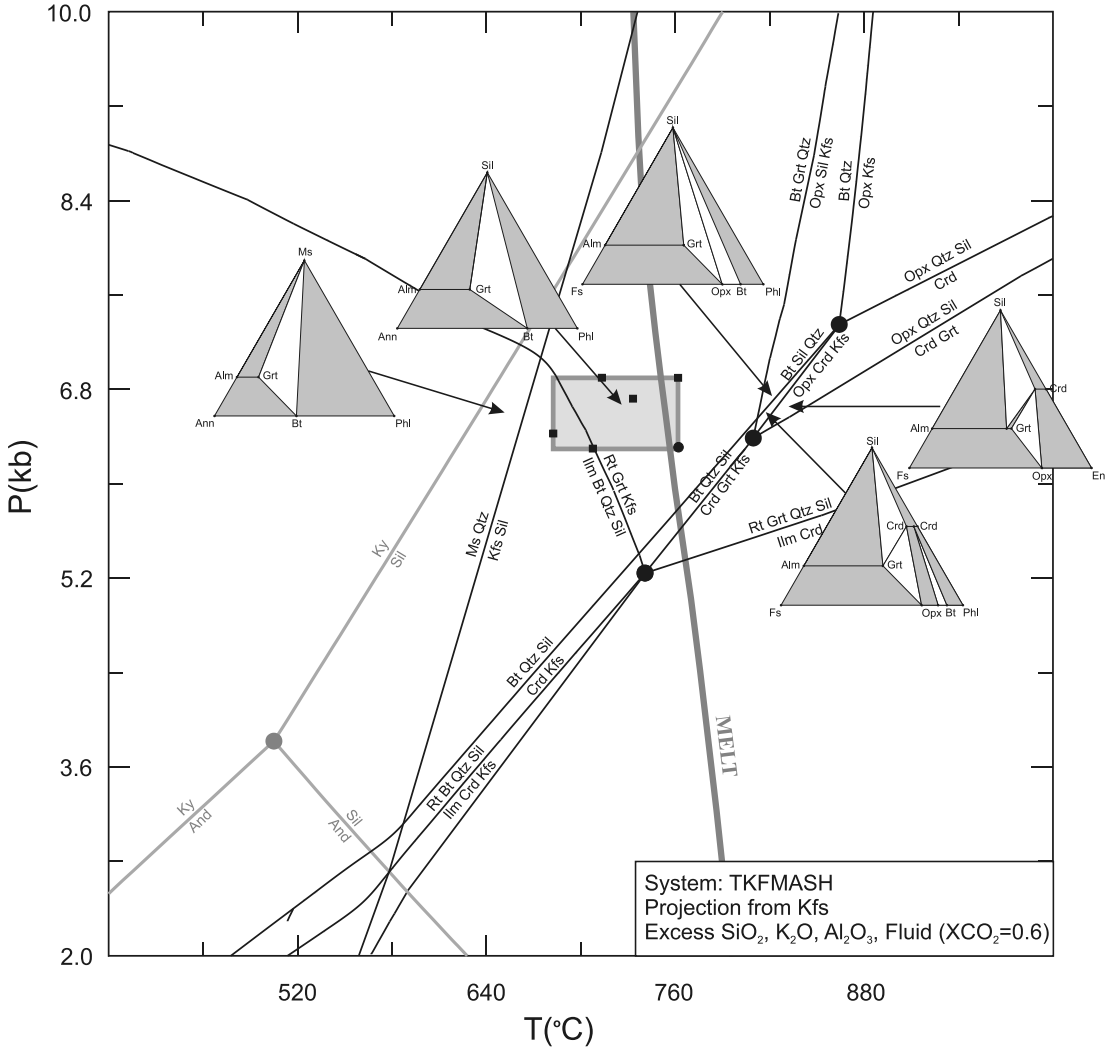

Fig. 9. Petrogenetic grid for basement mylonites adjacent to mafic–ultramafic bodies, constructed with updated version (2003) of PERPLEX program (Connolly and Kerrick, 1987; Connolly, 1990) using the thermodynamic database of Holland and Powell (1998). Rectangle with squares, P–T conditions determined from geothermobarometry. Small circle, lower right corner of rectangle, P–T conditions determined for mafic mylonite. MELT, granite solidus for XH_2O from Johannes and Holtz (1996). Al_2O_3 triple point after Holdaway (1971).

observations show that cordierite appears, without exception, intensively replaced by biotite + sillimanite. According to Hauzenberger et al. (2001), orthopyroxene is very rarely observed in metapelites and always occurs with an alteration rim of amphibole together with garnet, biotite, and feldspar. Thus, both phases are clearly retrogressed in mylonites. Considering that biotite + quartz + sillimanite and biotite + garnet + quartz are the observed equilibrium associations in basement mylonites adjacent to mafic–ultramafic bodies, the reactions biotite + quartz + sillimanite ⇆ cordierite + k-feldspar + H_2O and biotite + garnet + quartz ⇆ orthopyroxene + sillimanite + k-feldspar + H_2O (Fig. 9) establish the upper temperature limit for the mylonitization event. Petrographic evidence clearly indicates that mylonitization occurred after migmatite crystallization (neosomes are affected by the mylonitization event), which fixes an upper limit for the mylonitization event in the conditions of the granite melt solidus curve (MELT curve, Fig. 9), namely at approximately 760 °C with the estimated pressures and water activities.

All calculated temperatures for mylonites (including the mafic mylonite shown as a reference in Fig. 9) plot in the stability field of the associations observed in equilibrium during this event (rectangle with squares, Fig. 9). Thus, both phase relations and geothermobarometry indicate that the mylonitic deformation in mafic and adjacent country-rocks took place at high to very high temperatures, with conditions of upper amphibolite transitional to granulite facies and at intermediate pressures (Yardley, 1989; Spear, 1995).

Hauzenberger et al. (2001) determine pressures in the range 6.2–7.4 kbar for granulite facies assemblages at a reference temperature of 750 °C. They also establish temperatures in the range 745–825 °C by applying the geothermometers clinopyroxene–orthopyroxene, olivine–clinopyroxene, and olivine–spinel and using the cores of the phases of a weak deformed metagabbronorite. This temperature range agrees with the thermometric determinations on peridotites of the Pringles Metamorphic Complex (Ferracutti, personal commun.), with cooling temperatures in the range 780–790 °C. The *P–T* conditions representing the metamorphic peak are shown by a rectangle (M2-G) in Fig. 10.

As we show in Fig. 10, the established conditions of mylonitization for mafic–ultramafic and adjacent country-rocks are very close to the conditions reached during the metamorphic peak obtained by Hauzenberger et al. (2001). Thus, the mylonitic event probably developed not long after the emplacement of mafic–ultramafic bodies that caused granulite facies metamorphism and crustal anatexis.

However, the presence of mylonites bearing muscovite ± chlorite as stable phases in rocks distant from the mafic–ultramafic bodies (Hauzenberger et al., 2001) indicates that the mylonitization event developed on a sequence of rocks characterized by a thermal gradient generated during the mafic–ultramafic intrusion.

8. Discussion

8.1. Deformation mechanisms

Given that, for example, plagioclase and garnet in both mafic and country-rock mylonites behave in the same way during mylonitization, we analyze mineral-by-mineral deformation mechanisms together for all types of rocks to avoid unnecessary repetitions. Quartz, k-feldspar, sillimanite, and cordierite are present only in basement mylonites, whereas hornblende and orthopyroxene are found only in mafic mylonites.

8.1.1. Quartz

Quartz ribbon appearances can be compared with types B3 and B4 of Boullier and Bouchez (1978). The high grain boundary mobility within the ribbons usually occurs at very high temperatures (e.g., Simpson and De Paor, 1991), where the dominant deformation mechanism is grain boundary migration recrystallization (GBMR), and well above the beginning of the experimentally derived Regime 3 of Hirth and Tullis (1992). According to Stipp et al. (2002), in naturally deformed quartz-rich rocks, the transition from the subgrain rotation recrystallization (SGRR) mechanism to the dominant GBMR mechanism occurs at approximately 500 °C. Recrystallized grain sizes and 100% recrystallization indicate minimum temperatures for the mylonites of the CB of around 550 °C (Stipp et al., 2002).

8.1.2. Feldspars

The discrimination between SGRR- and GBMR-dominated microstructures is based mainly on the homogeneously flattened porphyroclasts, polygonization, new grains of similar size and intragranular strain to preexisting subgrains, and the development of core and mantle microstructures for SGRR versus the relatively unstrained irregular or rounded porphyroclasts with serrated boundaries, irregular new grain shapes (low-temperature deformations) to polygonal new grains with dissimilar sizes (high-temperature deformations), and variation in intragranular strain for GBMR (Poirier and Nicolas, 1975; White, 1976; Hobbs et al., 1976; Guillopé and Poirier, 1979; Means, 1983; Urai, 1983; Tullis and Yund, 1985; Hirth and Tullis, 1992; Lloyd and Freeman, 1994).

Textural characteristics observed for both k-feldspar and plagioclase indicate that the dominant deformation mechanism was GBMR. Evidence for GBMR can be summarized as follows: first, dominantly rounded or elliptic porphyroclasts (Figs. 3d, g, h, 4c–e, 5d, e), bulging from the borders or intracrystalline fractures that give rise to new grains separated from the relict by high-angle boundaries and no visible subgrain in the adjacent sector of the relict crystal (Figs. 4c–e, g, 55f); second, serrated and lobated boundaries between porphyroclasts and between recrystallized grains, suggesting high grain boundary mobility (Figs. 3c, 4e and f); and third, new grains with dissimilar

sizes, shapes, and intracrystalline deformation intensity (Figs. 4d, e, g, 5f). (Some plagioclase new grains show subhedral contours, straight twins, and lack of intracrystalline deformation, whereas others show undulatory extinction, lack of twins, and very irregular shapes with lobated boundaries; Fig. 5f.)

The presence of very scarce subgrains in k-feldspar porphyroclasts of some mylonitic bands indicates that SGRR has taken place at least incipiently in this mineral. Subgrains develop in the strongest strained crystalline sectors (borders, intracrystalline fractures) of rounded or elliptic porphyroclasts. The occurrence in some mylonitic samples of strongly flattened plagioclase crystals (Fig. 4g) showing kink bands, subgrains, or development of core and mantle structures containing polygonal new grains of the same size as the adjacent subgrains, indicate that climb was even more active in this mineral than in k-feldspar. This behavior is consistent with the fact that the activation energy of dynamic recrystallization and dislocation glide is lower for plagioclase than for K-feldspar in middle to high homologous temperatures (e.g., Fitz Gerald and Stunitz, 1993; Schulmann et al., 1996). Plagioclase new grains (up to 225 μm) formed by either GBMR or SGRR are greater than recrystallized matrix k-feldspar grains (50 μm), consistent with the preceding statement.

In summary, textural evidence indicates that both GBMR and SGRR deformation mechanisms contributed to dynamic recrystallization of feldspars, though the former clearly is dominant in most studied basement mylonites. Snoke et al. (1998) indicate that at natural strain rates, GBMR appears to be the dominant deformation mechanism in feldspars from about middle greenschist through middle to upper amphibolite facies conditions. The transition from GBMR and SGRR is not well understood (Tullis and Yund, 1991). Tullis and Yund (1985) suggest that in upper amphibolite and granulite facies rocks, feldspar usually exhibits subgrains and thus may undergo SGRR. Therefore, the observed deformation mechanisms for feldspar indicate high to very high temperatures for the mylonitic event.

K-feldspar porphyroclasts develop coarser subpolygonal new grains (up to 150–170 μm), mainly in borders facing pressure shadows and intracrystalline fractures, in contrast to the finer and more irregular new grains (50 μm) of the mylonitic matrix (compare Figs. 4c and d). This characteristic also is observed for recrystallized quartz grains. If fluids are present during deformation, they normally migrate to low-pressure sites. Trace amounts of water can profoundly affect the strength of silicates experimentally deformed by dislocation creep (Farver and Yund, 1990; Hirth and Tullis, 1992; Kronemberg and Tullis, 1994). The presence of a fluid phase enhances diffusion at the borders of the grains (diffusion creep, Tullis and Yund, 1991), favoring grain boundary migration and, consequently, the growth of recrystallized grains (Tullis and Yund, 1982; Hirth and Tullis, 1992). Therefore, dissimilar grain sizes of recrystallized grains in the matrix and extension sites could indicate the migration of fluids to low-pressure sites, favoring grain boundary migration and faster growth of new grains. This supposition is valid for the dissimilar grain sizes in synmylonitization neominerals (biotite and opaque phases), which are coarser grained in extension sites than in the surrounding matrix (e.g., Figs. 4a–c, 5d–g). Thus, partitioning deformation with different rheological responses between highly sheared domains and protected areas is apparent and generates different microstructures simultaneously.

Some mylonite basement samples have only plagioclase porphyroclasts. The presence of abundant neocrystallized biotite strongly suggests that in addition to the intense recrystallization, the shrinkage and disappearance of original k-feldspar porphyroclasts may be attributed to reactions to secondary biotite due to the presence of fluids during the mylonitic event. However, in other mylonite samples, plagioclase remnants are rarer than k-feldspar porphyroclasts. Both phases have undergone grain size reduction by recrystallization and chemical destabilization, due to the presence of fluids during the mylonitization. Although the described process could not have affected both phases with the same intensity, modal protolithic plagioclase could have been locally reduced by replacement (plagioclase is a common constituent of poikilitic inclusions in garnet and k-feldspar) during the migmatization of the gneisses developed prior to the mylonite event. Thus, the predominance of plagioclase or k-feldspar as porphyroclasts in different mylonitic bands could be an inherited premylonitization characteristic that reflects different degrees of melting and amounts of migmatitic neosomes.

8.1.3. Sillimanite

Sillimanite porphyroclasts reflect brittle behavior during mylonitic deformation. Long tabular crystals show fracturing orthogonal to their long dimension and redistribution of the fragments along the mylonite foliation (Fig. 3a). Some original rhomboidal porphyroclasts underwent rounding of their apex and acquired sigmoidal shapes, oriented to resemble mica fishes (Passchier and Trouw, 1996), often with development of pressure shadows.

8.1.4. Garnet

Garnet behaved in a brittle way during the mylonitic event, as shown by the presence of abundant intracrystalline fractures (Fig. 4b) and, occasionally, the disruption in small fragments redistributed along the mylonitic foliation (Fig. 3e). Almost perfect circular or slightly elliptical shapes of garnet porphyroclasts enclosed in a biotite-bearing matrix (Figs. 3g, h, and 4a) are attributed to smoothing and rounding of the original irregular porphyroclasts due to fluid-assisted reaction to biotite (±opaques) during porphyroclast rotation. Small, internally unfractured garnet are considered fragments of once larger crystals that were able to rotate freely in a softer matrix (fine recrystallized quartz and feldspars and newly formed biotite and opaques), without interactions with other equivalently sized

grains in an advanced stage. Subhedral small grains with poikilitic inclusions indicate that some of the separated fragments were able to grow during the mylonitization event and incorporated matrix constituents (Fig. 3e). Irregularly shaped original garnet grains elongated subparallel to foliation, deformed mainly by fracturing subparallel to the flow plane, are considered a consequence of an unfavorable shape and orientation for rotation, which favored fracturing with displaced crystal edges.

8.1.5. Biotite

Textural relationships show that most biotites are associated with the mylonitic event. They fill porphyroclast intracrystalline fractures and crystallize in pressure shadows (e.g., Figs. 3–5). These biotites do not show signs of intracrystalline deformation in most mylonites. However, some coarse tabular crystals show bending and kinking in S/C protomylonites. Very small, rounded or subhedral inclusions, apparently unrelated to intracrystalline fractures (original poikiloblast inclusions?) and observed in the centers of k-feldspar porphyroclasts, have been noted. Both inclusions and deformed biotite laths could be remnants of biotites formed prior to the mylonitic event. However, no remarkable optical or compositional differences between deformed and undeformed biotites are noticeable.

8.1.6. Cordierite

No fresh cordierite is recognized in the studied samples. Only porphyroclast shapes have been partially preserved after intense retrogression and replacement by synmylonitization mineralogy (Fig. 3f). Therefore, no evidence of deformation mechanisms is preserved.

8.1.7. Hornblende

Hornblende shows evidence of recrystallization and the absence of brittle fracturing, which suggest it was deformed mainly by dislocation creep. Rounded or elliptic porphyroclasts with serrated borders (Figs. 5d–g), associated with recrystallized grains separated from the relict by high-angle boundaries and without visible subgrains (Fig. 5h), point to GBMR as the dominant deformation mechanism. As with garnet porphyroclasts, the rounded to elliptic shape of the hornblende porphyroclasts can be attributed to a combination of recrystallization and smoothing and rounding due to fluid-assisted reaction to form neominerals (mainly biotite), combined with rotation of porphyroclasts during the mylonitic event.

8.1.8. Orthopyroxene

Orthopyroxene shows irregularly shaped porphyroclasts with slight undulatory extinction and bending of clinopyroxene exsolution lamellae and microfractures. Porphyroclasts recrystallized to aggregates of polygonal new grains, meeting at 120° triple junctions (Fig. 5i). These characteristics indicate that orthopyroxene has undergone ductile deformation by dislocation creep. The absence of subgrains and flattened porphyroclasts point to GBMR as the most probable recrystallization mechanism.

8.2. Remobilization of sulfides, platinum group minerals

Sulfides can be found elsewhere in the studied basement mylonites and mafic mylonite. Sulfide mineralogy (pyrrhotite, pentlandite, chalcopyrite, and pyrite) and oxides (ilmenite and magnetite) constitute up to 10–12% of the mafic mylonites and only 1% of the adjacent, almost undeformed mafic protolith. They are more abundant and develop greater sizes in basement mylonites near mafic–ultramafic bodies, decreasing in proportion and grain size away from the bodies where oxides (magnetite, ilmenite) predominate.

The concentration of sulfides in the mylonitic bands and their textural relationships (e.g., distribution along foliation planes, crystallization within porphyroclast extension sites, boudinaged grain fragments) provide unequivocal evidence of remobilization of primary magmatic sulfides of mafic–ultramafic rocks (+PGM) during the mylonitic event. Like other neominerals (biotite, oxides), sulfides crystallized in the extension sites develop greater sizes than those in the matrix and do not show evidence of deformation. Several examples of the characteristics and distribution of opaque minerals appear in Figs. 3–5.

8.3. Low-temperature event

A low-temperature event, separated from the mylonitic event, was first proposed by Delpino et al. (2002). This low-temperature final overprint produced brittle fracturing and localized retrogression on mafic–ultramafic minerals and ores, with serpentine + magnetite ± actinolite as the most representative association. Microfracturing affected mafic–ultramafic minerals and their recrystallization envelopes, which were generated during the mylonitization event. In ultramafic domains, continuous microcracks affecting relict and recrystallized olivine grains are sealed mainly by serpentine ± magnetite, as shown by Ferracutti and Bjerg (2002, Fig. 2a).

This low-temperature process is also recognized in the adjacent country rocks, where the mylonitic texture is locally obliterated along preexisting mylonitic foliation planes by a randomly oriented replacement of mylonite mineralogy by the assemblage chlorite + sericite/muscovite + magnetite. This low-temperature event is mainly responsible for the partial replacement of sulfides by oxides.

Some authors relate the low-temperature paragenesis to the mylonitic event in this central portion. Although later fluids associated with this low-temperature event seem to have moved, at least partially, along the pathways previously opened by the mylonitic event, the following characteristics argue against that interpretation: (1) There is clear evidence of obliteration of mylonitic textures and replacement of synmylonite mineralogical associations (Figs. 4h,

i); (2) low-temperature paragenesis is incompatible with the temperatures required to produce the observed ductile deformation in mylonitic minerals of this sector; and (3) well-constrained P–T conditions obtained through equilibrated synmylonitic paragenesis are above the stability field of low-grade paragenesis, and some phases, such as serpentine, are not stable in the determined range of fluid composition.

8.4. Origin of fluids

The fluid phases accompanying the metamorphic peak, the mylonitic event, and the low-temperature event differ compositionally.

Through microthermometric investigations and Raman spectroscopy on primary fluid inclusions from metapelites and gabbronorites, Felfernig et al. (1999) establish that granulite facies peak metamorphic fluids are nearly pure CO_2, with small amounts of CH_4 and N_2. Calculated isochors for these primary fluid inclusions (Fig. 3 in Felfernig et al., 1999) give pressures of 6–7 kbar for the peak metamorphic temperature range of 745–825 °C calculated by Hauzenberger et al. (2001) with classical geothermometers and geobarometers to mineral cores of gabbronorites. This pressure range agrees with that calculated by these authors (6.2–7.4 kbar) and confirms that these fluid inclusions represent the composition of the fluid phase accompanying the metamorphic peak.

Internally consistent geothermobarometry applied to the mineralogical associations equilibrated during the mylonitic event suggests fluid compositions ranging from $0.3 < XCO_2 < 0.7$ (most values between 0.5 and 0.6) for basement mylonites to $XCO_2 = 0.89$ for mafic mylonites (Figs. 7 and 8). The migmatization of basement rocks around mafic–ultramafic bodies has been attributed to the intrusion of these high-temperature magmatic rocks. Because the generation of in situ granitic melts usually consumes water but rejects carbon dioxide (e.g., Carrol and Holloway, 1994; Clemens et al., 1997), this situation may have contributed to the generation of an almost pure CO_2 residual fluid phase. Further crystallization of neosomes during cooling liberated water-rich fluids. The determined P–T conditions for the mylonitic event are close to and under the granite melt solidus (Fig. 9), so the crystallization of migmatite neosomes and granitic segregates represent a suitable source for the fluid phase accompanying the mylonitic event. Intense deformation of the preexisting phases could have contributed to the liberation of CO_2-rich fluids trapped in fluid inclusions. Further mixing with water-rich fluids released from the crystallization of neosomes would give rise to the mixed CO_2–H_2O fluids found in mylonites. Because both neosome proportions and deformation intensities are variable, this characteristic could explain the variable range of compositions of the fluid phases accompanying the mylonitic event. A more constant composition would be expected for fluid supplied by an external source; therefore, this compositional variability also could support in situ generation of this fluid phase.

The crystallization of serpentine during the low-temperature event indicates the presence of a water-rich fluid phase, because this mineral is stable only with very high-water activities. At a fluid pressure of 1 kbar, serpentine is stable at $XCO_2 < 0.1$, and its stability field is displaced even to lower XCO_2 values with increasing pressures (e.g., Yardley, 1989; Spear, 1995). Thus, serpentine could not be stable in the range of fluid phase compositions determined for the mylonitic event, and another source must be invoked. A suitable source for a water-rich fluid phase could be the large, undeformed, postkinematic plutons (Las Chacras–Piedras Coloradas, El Volcán, La Totora) that span the Devonian–Early Carboniferous interval and whose emplacement was fracture controlled (Brogioni, 1987, 1992, 1993; López de Luchi, 1993; Llambías et al., 1998; von Gosen et al., 2002).

8.5. Physical conditions of mylonitic event: implications for constructing a P–T–d path

Textural evidence and mineral chemistry indicate that both mafic and adjacent basement mylonites attained chemical equilibrium during deformation and did not experience, other than locally, retrogression during cooling. High to very high temperatures and the presence of a fluid phase during mylonitization could facilitate intracrystalline diffusion rates and reaction kinetics to attain equilibration in the imposed P–T–X_f conditions. As we discussed previously, this possibility is indicated by the differences in the chemical compositions of porphyroclasts of mafic mylonites and their parental phases of the immediately adjacent and almost undeformed noritic protolith. Relict and recrystallized hornblende, plagioclase, and orthopyroxene grains within mafic mylonites do not show noticeable chemical differences. Hence, porphyroclast compositions were fully reseated to match the prevailing conditions during the mylonitic event.

The P–T obtained for mafic mylonites and adjacent basement mylonites (6.28–6.85 kbar, 687–762 °C) of the central sector of the Pringles Metamorphic Complex indicate conditions of deformation in the upper amphibolite transitional to granulite facies with medium pressures. These conditions are consistent with the stable presence of orthopyroxene (unaltered porphyroclasts and fine-recrystallized grains) in mafic mylonites. However, the following basement mylonites were recognized from the extremes of the shear zone to the mafic–ultramafic central bodies: lower amphibolite facies (muscovite + k-feldspar$_1$ + plagioclase + quartz + biotite ± garnet ± chlorite; M3-Ph of Hauzenberger et al., 2001) ⇒ middle amphibolite facies (garnet + biotite + muscovite + plagioclase + quartz + sillimanite; M3-A of Hauzenberger et al., 2001) ⇒ upper amphibolite transitional to granulite facies (garnet + biotite + k-feldspar$_2$ + plagioclase + quartz + sillimanite and garnet + biotite + plagioclase + hornblende +

orthopyroxene; basement and mafic mylonites, respectively, this contribution). Garnet–biotite thermometry on lower (M3-Ph) and middle (M3-A) amphibolite facies mylonites indicate temperatures of 555 °C and 585–680 °C, respectively (Hauzenberger et al., 2001). Thus, a temperature gradient from 555 °C to 762 °C can be estimated for the mylonitic event that affected the Pringles Metamorphic Complex.

These characteristics strongly suggest that the mylonitization event developed on a geothermal gradient generated by the intrusion of mafic–ultramafic bodies. This interpretation is supported by the *P–T* conditions of mylonitization determined for mafic and adjacent basement mylonites (668–764 °C, 6.3–6.9 kbar), very close to peak metamorphic conditions (745–825 °C, 6.2–7.4 kbar) determined by Hauzenberger et al. (2001).

Therefore, if a wide temperature metamorphic gradient was present during the mylonitization event, we must be cautious in assigning unique physical conditions to this tectonothermal event and in constructing the *P–T* path for the tectonometamorphic evolution of the area. Because rock units located marginal to the central portion never reached metamorphic peak temperatures, more than one *P–T* path is required to represent the trajectories followed by the rock units located at different distances from the mafic–ultramafic bodies. We provide two probable paths in Fig. 10.

Both progressive trajectories start within the andalusite stability field; according to von Gosen (1998), chiastolite formed as a result of contact metamorphism on undeformed metapelites due to the intrusion of tonalitic bodies, considered of early Famatinian age (Llambías et al., 1998).

Path 1, essentially constructed from our data and observations, describes the behavior of basement rocks adjacent to mafic–ultramafic bodies that have reached anatexis conditions within granulite facies. It comprises migmatitic gneisses with k-feldspar, cordierite, orthopyroxene, and coarse prismatic sillimanite, on which upper amphibolite transitional to granulite facies mylonites develop. The reconstructed *P–T* trajectory is based on the following aspects: peak metamorphic conditions must be above Crd and Opx stability fields and the beginning of melting in metapelitic rocks, and garnet shows poikiloblastic growth at the expense of cordierite and ilmenite and, therefore, the reaction ilmenite + cordierite ⇆ rutile + garnet + quartz + sillimanite is crossed in the sense of increasing pressures. Although orthopyroxene is extremely rare in relation to cordierite, its presence indicates that the metamorphic path must pass through the stability field of this phase. Thus, the invariant point [2] fixes the minimum *P–T* conditions reached by these rocks. This trajectory is consistent with the *P–T* conditions for the metamorphic peak obtained by geothermobarometry (M2-G, Fig. 10). During retrogression, the orthopyroxene and cordierite phases are retrograded, and the stable assemblages in the higher-grade mylonites are: biotite + quartz + sillimanite and biotite + quartz + garnet. Therefore, the metamorphic trajectory must cross the reactions biotite + quartz + sillimanite ⇆ cordierite + k-feldspar + H_2O and biotite + garnet + quartz ⇆ orthopyroxene + sillimanite + k-feldspar + H_2O, in the sense of decreasing temperatures. Moreover, mylonitization must occur at higher temperatures than those corresponding to the conditions of the reaction muscovite + quartz ⇆ k-feldspar + sillimanite + H_2O (second sillimanite isograd), which mark the upper stability of muscovite, absent in these rocks, consistent with the obtained geothermobarometric results.

Path 2, which is based essentially on published references in combination with our observations, describes the behavior of rocks that, having undergone thermal input due to the intrusion of mafic–ultramafic bodies, have not reached conditions for anatexis. These rocks are mylonitized gneisses composed of garnet + biotite + muscovite + plagioclase + quartz ± staurolite ± sillimanite (Hauzenberger et al., 2001). Chlorite is also present but appears as partly concordant and partly discordant grains in relation to foliation, and thus, a younger origin can not be excluded. The total absence of k-feldspar indicates that the upper stability limit for muscovite (second sillimanite isograd) was never exceeded during the progressive stage. The overlapped mylonitization on retrogression has muscovite and garnet as stable phases and a lack of k-feldspar, indicating that mylonitization did not reach the *P–T* conditions of the second sillimanite isograd. The thermal maximum indicated by thermobarometry for mylonites developed from these protoliths (M3-A, Fig. 10), which corresponds with the minimum temperatures obtained for the higher-grade mylonites (HGM, Fig. 10) indicate a continuous gradation, though average estimated pressures appear more or less in the same range. Lower-grade mylonites include chlorite. As we observed in the higher-grade mylonites, textural relations indicate that chlorites usually show random growth at the expense of biotite, which, together with muscovite, depicts mylonitic foliation (von Gosen, 1998). In Fig. 10, chlorite is not stable in the range of *P–T* conditions obtained through geothermobarometry except with very high water activities. Thus, most chlorites could have been formed during the later low-temperature event, together with muscovite–sericite. The reaction chlorite + muscovite ⇆ biotite + quartz + silimanite + H_2O ($XH_2O = 1.0$) in Fig. 10 represents the retrogression of the stable assemblage in mylonites in the presence of a water-rich fluid phase, as we estimated for the low-temperature event, and approximately marks the upper limit for this later event.

Absence of kyanite precludes the possibility that the final stage of retrograde Path 2 passed through the stability field of this phase. However, the lack of muscovite in higher-grade mylonites indicates that the second sillimanite isograd was not crossed on retrogression by Path 1, which suggests rapid exhumation of the whole sequence and therefore may contribute to the preservation of medium pressure assemblages. This trajectory is consistent with a scenario characterized by decompression and cooling during postcollisional crustal uplift, as proposed for the origin of postorogenic

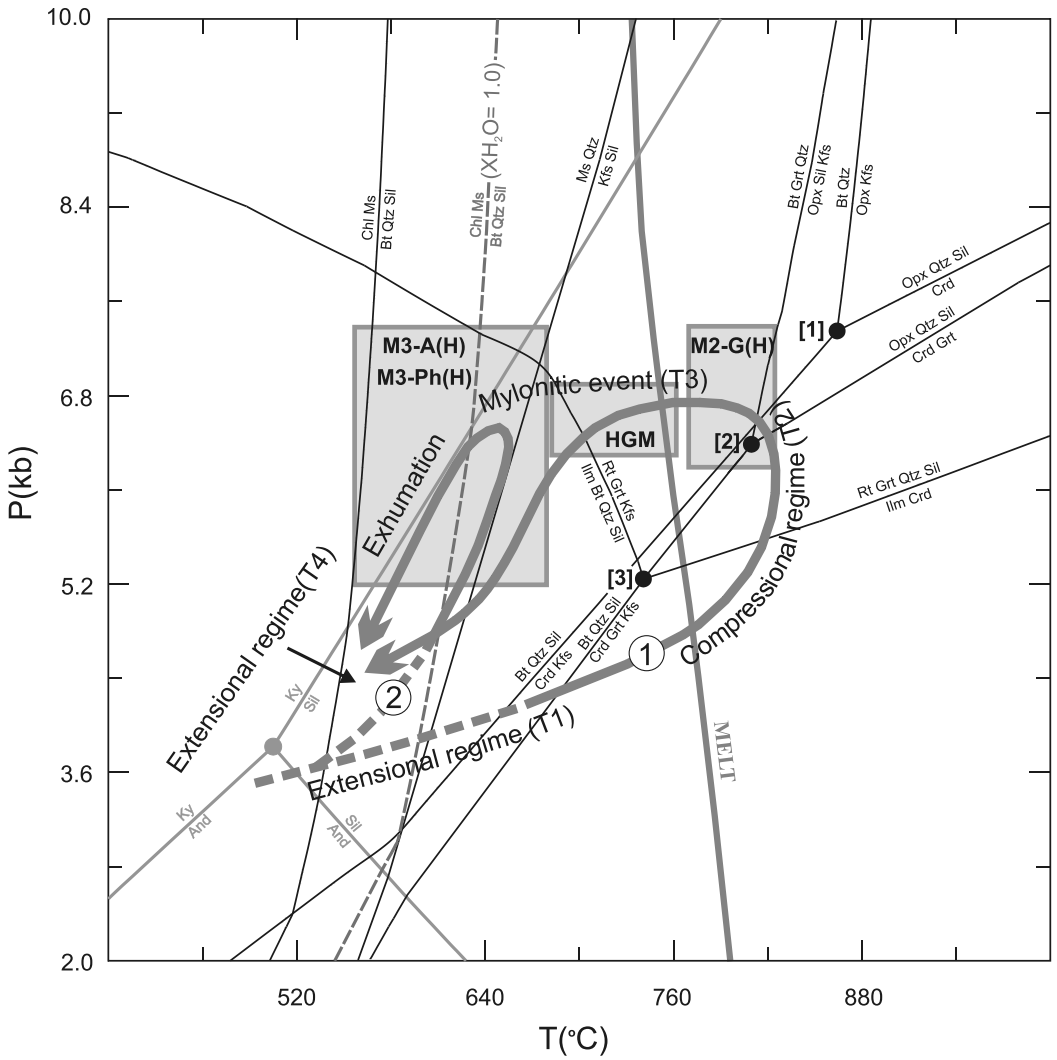

Fig. 10. Proposed *P–T–d* paths for evolution of Pringles Metamorphic Complex. HGM, *P–T* conditions for higher-grade mylonites close to mafic–ultramafic bodies. M3-A(H)/M3-Ph(H), *P–T* conditions for lower-grade mylonites away from mafic–ultramafic bodies (Hauzenberger et al. (2001). M2-G(H), *P–T* conditions for the metamorphic peak (Hauzenberger et al., 2001). MELT, granite solidus for XH_2O from Johannes and Holtz (1996). Al_2O_3 triple point after Holdaway (1971).

batholiths by López de Luchi (1996) and Llambías et al. (1998). Rising during extensional collapse, epizonal (fracture-controlled) emplacement (Brogioni, 1993) at about 4–5 kbar (López de Lucchi, 1993), and crystallization of the bodies offers a suitable source of water-rich fluids for the later (localized) low-temperature event.

8.6. Succession of tectonometamorphic events

On the basis of our previous and present work and published data, we propose the following succession of tectonometamorphic events for the evolution of the Pringles Metamorphic Complex:

1. T_1–M_1 (extensional regime): A N–S trending rift opened, and sedimentation (530 Ma based on U–Pb zircon core detrital ages from pelitic gneisses of Pringles Metamorphic Complex, Sims et al., 1998) was followed by the intrusion of tonalitic bodies (Early Famatinian, Late Cambrian–Early Ordovician pre-orogenic granitoids, Llambías et al., 1998). Crustal thinning, mantle upwelling, and emplacement of layered mafic–ultramafic bodies (478 Ma, magmatic crystallization age for Las Águilas intrusion, Sims et al., 1998) led to isotherm rising, metamorphism, and crustal anatexis of pelitic sediments, as well as the generation of migmatites and anatectic melts and the establishment of a geothermal gradient from greenschist to granulite facies. This first stage is similar to that proposed by Bohlen (1987) for trajectories characterized by isobaric cooling paths (IBC), where magma underplating in an extensional regime produces granulite facies metamorphism.
2. T_2–M_2 (early compressional regime): Crustal thickening associated with regional folding with steeply dipping axes (b_2) affecting S_0 and the migmatitic layering, and the development of an axial plane foliation (S_2).

S-type anatectic granites–granodiorites were emplaced (Famatinian, Ordovician, early to synorogenic granitoids, Llambías et al., 1998).

3. T_3–M_3 (late compressional regime): A wide NNE–SSW–trending shear zone developed with reverse (top to WNW) displacement, associated with folding with subhorizontal axes (b_3) and the development of the S_3 (mylonitic) foliation. The conditions of mylonitization grade from upper amphibolite to granulite in the center of the CB to lower amphibolite facies near the eastern and western extremes.
4. T_4–M_4 (extensional regime): Postorogenic extensional collapse and emplacement of fracture-controlled, undeformed postorogenic granitoids occurred (Late Famatinian, Devonian–Early Carboniferous granitoids, Brogioni, 1993; López de Luchi, 1996; Llambías et al., 1998), after a rapid exhumation of the sequence. Low-temperature retrogression (greenschist facies) channelized along brittle fractures and preexisting S_2-S_3 foliation planes.

The most likely geological setting for this type of evolution is a backarc basin, as suggested by Ramos (1988), Sims et al. (1998), Hauzenberger et al. (2001), and López de Luchi et al. (2003).

9. Conclusions

Petrogenetic grid and geothermobarometry applied to paragenesis equilibrated during the mylonitic event, together with mineral deformation mechanisms, indicate that mafic and adjacent basement mylonites developed under upper amphibolite transitional to granulite facies conditions of metamorphism at intermediate pressures (668–764 °C, 6.3–6.9 kbar, $0.3 < XCO_2 < 0.7$).

A temperature gradient of 555–764 °C and pressures of 6–7 kbar can be established for the mylonitic event from the external limits of the Pringles Metamorphic Complex to its center (mafic–ultramafic bodies): lower-amphibolite facies mylonites (muscovite + k-feldspar$_1$ + plagioclase + quartz + biotite ± garnet ± chlorite) ⇒ middle amphibolite facies (garnet + biotite + muscovite + plagioclase + quartz + sillimanite) ⇒ upper amphibolite transitional to granulite facies (basement: garnet + biotite + k-feldspar$_2$ + plagioclase + quartz + sillimanite; mafic: garnet + biotite + plagioclase + hornblende + orthopyroxene). Therefore, the mylonitic event developed on a preexisting temperature gradient caused by the intrusion of mafic–ultramafic bodies.

The concentration of sulfides in mylonitic bands and the textural relationships (distribution along foliation planes, crystallization within porphyroclast extension sites) provide undisputed evidence of remobilization of primary magmatic sulfides of the mafic–ultramafic rocks (+PGM) during the mylonitic event.

A low-temperature final overprint produced brittle fracturing and localized retrogression on mafic–ultramafic minerals and ores by means of a water-rich fluid phase, which formed a serpentine + magnetite ± actinolite assemblage. Concordantly, in the adjacent country-rocks, fluids channeled along preexisting mylonitic foliation planes and locally obliterated the mylonitic texture by a randomly oriented replacement of the mylonite mineralogy by the assemblage chlorite + sericite/muscovite + magnetite.

Observed mineral reactions combined with structural data and geothermobarometry enable us to propose a counterclockwise *P–T–d* path for the tectonometamorphic evolution of the Pringles Metamorphic Complex. The first stage of the trajectory (T_1–M_1) is characterized by rifting in an extensional regime, early intrusion of tonalitic bodies, and emplacement of mafic–ultramafic bodies, which produce granulite facies metamorphism and crustal anatexis. This low-pressure/high-temperature stage is followed by a compressional stage with crustal thickening in a collisional setting (early T_2–M_2). A postpeak period of isobaric cooling (late T_3–M_3) is followed by rapid exhumation of the sequence and a final extensional regime (T_4–M_4) associated with the intrusion of undeformed granitoids and local retrogression of the sequence. The most likely geological setting for this type of evolution is a backarc basin, associated with east-directed Famatinian subduction initiated in Mid-Cambrian times (Dalla Salda et al., 1992; Pankhurst et al., 1998), that closed during the collision of the allochthonous Precordillera terrane in Mid-Ordovician times (Dalla Salda et al., 1992; Ramos et al., 1998).

Acknowledgements

This work was supported by SCyT-UNS (Argentina) Grants 24/H042 and 24/H066 to EAB and by FWF Project (P10623-TEC) to AM. We thank Kurt Krenn of the University of Graz, Austria, for corrections of the initial draft of the manuscript. We also thank Dr. P. Gonzalez and an anonymous reviewer, whose comments were of great help to improve this manuscript.

References

Aceñolaza, F., Toselli, A., 1976. Consideraciones estratigráficas y tectónicas sobre el Paleozoico inferior del Noroeste Argentino. II Congreso Latinoamericano de Geología Memorias 2, 755–763.

Astini, R., 1996. Las fases diastróficas del Paleozoico Medio en la Precordillera del oeste Argentino – Evidencias estratigráficas -. XIII Congreso Geológico Argentino y III Congreso de Exploración de Hidrocarburos 5, 509–526.

Astini, R., Benedeto, J., Vaccari, N., 1995. The Early Paleozoic evolution of the Argentine Precordillera as a Laurentia Rifted , drifted, and collided terrane –a geodynamic model. Geological Society of America Bulletin 107, 253–273.

Berman, R.G., 1988. Internally-consistent thermodynamic data for minerals in the system Na_2O, K_2O, CaO, MgO, FeO, Fe_2O_3, Al_2O_3, SiO_2, TiO_2, H_2O, CO_2. Journal of Petrology 29, 445–522.

Berman, R.G., 1991. Thermobarometry using multi-equilibrium calculations: a new technique, with petrological applications. Canadian Mineralogist 29, 833–855.

Berman, R.G., Aranovich, L.Y., 1996. Optimized standard state and solution properties of minerals I. Model calibration for olivine,

orthopyroxene, cordierite, garnet, and ilmenite in the system FeO–MgO–CaO–Al_2O_3–TiO_2–SiO_2. Contribution to Mineralogy and Petrology 126, 1–24.

Berman, R.G., Aranovich, L.Y., Pattison, D.R.M., 1995. Reanalysis of the garnet–clinopyroxene Fe–Mg exchange thermometer. II. Thermodynamic analysis. Contribution to Mineralogy and Petrology 119, 30–42.

Berthe, D., Choukroune, P., Jegouzo, P., 1979. Orthogneiss, mylonites and non-coaxial deformation of granites: The example of the South Armorican shear zone. Journal of Structural Geology 1, 31–42.

Bjerg, E.A., Delpino, S., Dimieri, L., Kostadinoff, J., Mogessie, A., Hoinkes, G., Hauzenberger, Ch. A. and Felfernig, A., 1997. Estructura y Mineralizaci6n del Area Las Águilas – Virorco, San Luis, Argentina. VIII Congreso Geologico Chileno, Actas 2: 857–861. Santiago.

Bohlen, S.R., 1987. Pressure–temperature–time paths and a tectonic model for the evolution of granulites. Journal of Geology 95, 617–632.

Boullier, A.M., Bouchez, J.L., 1978. Le quartz en rubans dans les mylonites. Bulletin de la Société Géologique de France 7, 253–262.

Brogioni. N., 1987. El Batolito de Las Chacras-Piedras Coloradas, San Luis Geología y edad, X Congreso Geológico Argentino, Actas 4: 115–118, Tucumán.

Brogioni, N., 1992. El cuerpo máfico-ultramáfico de Las Águilas, provincia de San Luis. Mineralogía de los silicatos. I Reunión de Mineralogía y Metalogenia y I Jornada de Mineralogía, Petrografía y Metalogénesis de Rocas Ultrabásicas, Actas 379–392, La Plata.

Brogioni, N., 1993. El batolito de Las Chacras-Piedras Coloradas, Provincia de San Luis. Geocronología Rb–Sr y ambiente tectónico. XII Congreso Geológico Argentino y II Congreso de Exploración de Hidrocarburos, Actas 4: 54–60, Mendoza.

Brogioni, N., 1994. Petrología de la faja de rocas máficas y ultramáficas de la Sierra de San Luis, Argentina. VII Congreso Geológico Chileno, Actas 2: 967–971, Concepción.

Brogioni, N., 2001. Geología de los cuerpos Virorco y El Fierro, faja máfica-ultramáfica del borde oriental de la Sierra de San Luis. Revista de la Asociación Geológica Argentina 56 (3), 281–292.

Brogioni, N., Ribot, A., 1994. Petrología de los cuerpos La Melada y La Gruta, faja máfica-ultramáfica del borde oriental de la Sierra de San Luis. Revista de la Asociación Geológica Argentina 49, 269–283.

Bucher, K., Frey, M., 1994. Petrogenesis of Metamorphic Rocks. Springer-Verlag, Berlin, 318pp.

Caminos, R., 1973. Some granites, gneisses and metamorphites of Argentina. En: Lister, L. A. (Ed.), Symposium on Granites, Gneisses and Related Rocks. Geological Society, South Africa, Special Publication, 3: 333–338.

Caminos, R., 1979. Sierras Pampeanas Noroccidentales de Salta, Tucumán Catamarca, La Rioja y San Juan. Segundo Simposio de Geología Regional Argentina. Academia Nacional de Ciencias, Córdoba 1, 225–291.

Carrol, M., Holloway, J., 1994. Volatiles in magmas. Reviews in Mineralogy: 30, Mineralogical Society of America, Washington, DC.

Clemens, J., Droop, G., Stevens, G., 1997. High-grade metamorphism, dehydration and crustal melting: a reinvestigation based on new experiments in the silica-saturated portion of the system $KAlO_2$–MgO–SiO_2–H_2O–CO_2 at $P \leqslant 1.5$ Gpa. Contribution to Mineralogy and Petrology 129, 308–325.

Connolly, J.A.D., 1990. Multivariable phase-diagramas – an algorithm based on generalized thermodynamics. American Journal of Science 290, 666–718.

Connolly, J.A.D., Kerrick, D.M., 1987. An algorithm and computer program for calculating composition phase diagrams. CALPHAD 11, 1–55.

Cucchi, R.J., 1964. Análisis estructural de cuarcitas y granulitas bandeadas miloníticas de la Sierra de San Luis. Revista de la Asociación Geológica Argentina 19, 135–150.

Dalla Salda, L., 1987. Basement tectonics of the Southern Pampean Ranges, Argentina. Tectonics 6, 249–260.

Dalla Salda, L., Cingolani, C., Varela, R., 1992. Early Paleozoic orogenic belt of the Andes in southwestern South America: Result of Laurentia–Gondwana collision? Geology 20, 617–620.

Delpino, S., Dimieri, L., Bjerg, E., Kostadinoff, J., Mogessie, A., Hoinkes, G., Hauzenberger, Ch., Felfernig, A., 2001. Geometrical analysis and timing of structures on mafic–ultramafic bodies and high-grade metamorphic rocks, Sierras Grandes of San Luis, Argentina. Journal of South American Earth Sciences 14 (1), 101–112.

Delpino, S., Bjerg, E., Ferracutti, G., Dimieri, L., Mogessie, A., Kostadinoff, J., 2002. Upper-amphibolite facies mylonitization of mafic–ultramafic rocks and gneissic–migmatitic country rocks, Sierras de San Luis, Argentina: implications in the remobilization of ore sulfides. VI Congreso de Mineralogía y Metalogenia: 123–126, Buenos Aires.

Farver, J.R., Yund, R.A., 1990. The effect of hydrogen, oxigen and water fugacity on oxigen diffusion in alkali feldspar. Geochimica et Cosmochimica Acta 54, 2953–2964.

Felfernig A., Mogessie, A., Hauzenberger, C., Hoinkes, G., Loizenbauer, J., Bjerg, E., Kostadinoff, J., Delpino, S., Dimieri, L., 1999. The role of fluids in platinum mineralization of the mafic–ultramafic Las Águilas complex, San Luis province, Argentina. Actas 14 Congreso Geológico Argentino 2: 287–289. Salta, Argentina.

Ferracutti, G., Bjerg, E., 2002. Relación entre mineralización y deformación en rocas máficas-ultramáficas del yacimiento Las Águilas, Provincia de San Luis, Argentina. En: Cabaleri, N., Cingolani, C., Linares, E., López de Luchi, M., Ostera, H., Panarello, H. (Eds.), XV Congreso Geológico Argentino CD-ROM. Artículo No. 014, 6pp.

FitzGerald, J.D., Stunitz, H., 1993. Deformation of granitoids at low metamorphic grade. I; Reactions and grade size reduction. Tectonophysics 221, 269–297.

González, P. D., Sato, A. M., Basei, M. A., Vlach, R. F. y Llambías, E. J., 2002. Structure, metamorphism and age of the Pampean–Famatinian Orogenies in the western Sierra de San Luis, XV Congreso Geológico Argentino (CD), El Calafate.

González Bonorino, F., 1961. Petrología de algunos cuerpos básicos de San Luis y las granulitas asociadas. Revista de la Asociación Geológica Argentina 16 (1–2), 61–106.

Guillopé, M., Poirier, J.P., 1979. Dynamic recrystallization during creep of single-crystalline halite: an experimental study. Journal of Geophysical Research 84, 5557–5567.

Hauzenberger, Ch. A., 1997. The Sierras de San Luis, Central-Argentina metamorphic, metallogenic and geochemical investigations. Ph.D. thesis, Karl-Franzens Universität, Graz, Austria, 200pp.

Hauzenberger, Ch. A., Mogessie, A., Hoinkes, G., Bjerg, E. A., Kostadinoff, J., Delpino S. and Dimieri, L., 1997. Platinum Group Minerals in the Basic to Ultrabasic Complex of the Sierras de San Luis, Argentina. In: H. Papunen (Ed), Mineral Deposits: Research and Explorations – Where Do They Meet: 439–442. A. A. Balkema, Rotterdam.

Hauzenberger, Ch. A., Mogessie, A., Hoinkes, G., Felfernig, A., Bjerg, E. A., Kostadinoff, J., Delpino, S., Dimieri, L., Raniolo A., 1998. Metamorphic Evolution of the Southern Part of the Sierras de San Luis, Argentina. IV Reunión de Mineralogía y Metalogenia y IV Jornadas de Mineralogía, Petrología y Metalogénesis de Rocas Máficas y Ultramáficas: 121–130, Bahía Blanca.

Hauzenberger, Ch.A., Mogessie, A., Hoinkes, G., Felfernig, A., Bjerg, E.A., Kostadinoff, J., Delpino, S.y., Dimieri, L., 2001. Metamorphic evolution of the Sierras de San Luis: Granulite facies metamorphism related to mafic intrusions. Mineralogy and Petrology 71 (1/2), 95–126.

Hirth, G., Tullis, J., 1992. Dislocation creep regimes in quartz aggregates. Journal of Structural Geology 14, 145–159.

Hobbs, B.E., Means, W.D., Williams, P.F., 1976. An Outline of Structural Geology. John Wiley & Sons, New York, 571pp.

Holdaway, M.J., 1971. Stability of andalusite and the aluminum silicate phase diagram. American Journal of Science 271, 97–131.

Holland, T.J.B., Powell, R., 1998. An internally consistent thermodynamic data set for phases of petrological interest. Journal of Metamorphic Geology 16, 309–343.

Johannes, W., Holtz, F., 1996. Petrogenesis and Experimental Petrology of Granitic Rocks. Springer Berlin Heidelberg, New York.

Kostadinoff, J., Bjerg, E., Delpino, S., Dimieri, L., Mogessie, A., Hoinkes, G., Hauzenberger, Ch., Felfernig, A., 1998a. Gravimetric and magnetometric anomalies in the Sierras Pampeanas of San Luis. Revista de la Asociación Geológica Argentina 53 (4), 549–552.

Kostadinoff, J., Bjerg, E A., Dimieri, L., Delpino, S., Raniolo, A., Mogessie, A., Hoinkes, G., Hauzenberger, Ch. A., Felfernig, A., 1998b. Anomalías geofísicas en la faja de rocas máficas-ultramáficas de la Sierra Grande de San Luis, Argentina. IV Reunión de Mineralogía y Metalogenia y IV Jornadas de Mineralogía, Petrografía, Metalogénesis de Rocas Máficas y Ultramáficas, Actas 139–146, Bahía Blanca.

Kronemberg, A.K., Tullis, J., 1994. Flow strengths of quartz aggregates: grain size and pressure effects due to hydrolytic weakening. Journal of Geophysical Research 89, 4281–4297.

Lira, R., Kirschbaum, 1990. Geochemical evolution of granites from the Achala batholith of the Sierras Pampeanas, Argentina. In: Kay, S., Rapela, C. (Ed.), Plutonism from Antartica to Alaska. Geological Society of America Special Papers, 241: 67–76.

López de Luchi, M., 1993. Caracterización geológica y emplazamiento del batolito de Renca XII Congreso Geológico Argentino y II Congreso de Exploración de Hidrocarburos, Actas 4: 42–53, Mendoza.

López de Luchi, M., 1996. Enclaves en un batolito postectónico: petrología de los enclaves microgranulares del batolito de Renca, Sierras Pampeanas, San Luis. Revista de la Asociación Geológica Argentina 51 (2), 131–146.

López de Luchi, M., Cerredo, M., Siegesmund, S., Steenken, A., Wemmer, K., 2003. Provenance and tectonic setting of the protoliths of the Metamorphic Complexes of the Sierra de San Luis. Revista de la Asociación Geológica Argentina 58 (4), 525–540.

Llambías, E., Sato, A., Ortiz Suárez, A., Prozzi, C., 1998. The granitoids of the Sierra de San Luis. In: Pankhurst, R. J., Rapela, C. W. (Ed.), The Proto-Andean Margin of Gondwana. Geological Society, London, Special Publication 142: 325–341.

Lloyd, G.E., Freeman, B., 1994. Dynamic recrystallization of quartz under greenschist conditions. Journal of Structural Geology 16, 867–881.

Malvicini, L., Brogioni, N., 1993. Petrología y génesis del yacimiento de Ni, Cu y Platinoideos Las Águilas Este, provincia de San Luis. Revista de la Asociación Geológica Argentina 48 (1), 3–20.

Malvicini, L., Brogioni, N., 1996. Las Águilas Este deposit: Shear zone hosted hydrothermal Cu–Ni sulfide and platinum-group elements mineralization in the mafic–ultramafic complex of San Luis Range, Argentina. En: Coyner, A. R. y Fahey, P. L. (Ed.), Geology and Ore Deposits of the American Cordillera. Geological Society, Nevada, Symposium Proceedings: 1475–1485.

Means, W.D., 1983. Microstructure and micromotion in recrystallization flow of octachloro propane: a first look. Geologische Rundschau 72, 511–528.

Mogessie, A., Hoinkes, G., Stumpfl, E.F., Bjerg, E.A., Kostadinoff, J., 1994. The Petrology and Mineralization of the Basement and Associated Mafic–Ultramafic Rocks, San Luis Province, Central Argentina. Mitteilungen der Österreichischen Mineralogischen Gesellschafl 139, 347–348. Austria.

Mogessie, A., Hoinkes, G., Stumpfl, E. F., Bjerg, E. A., Kostadinoff, J., 1995. Occurrence of Platinum Group Minerals in the Las Águilas Ultramafic Unit within a Granulite Facies Basement, San Luis Province, Central Argentina. In: J. Paiava, B. Ktibek, and K. Zak (eds), Mineral Deposits: From Their Origin to Their Environmental Impacts: 897–900. A. A. Balkema, Rotterdam.

Mogessie, A., Hauzenberger, Ch. A., Hoinkes, G., Felfernig, A., Bjerg, E. A. and Kostadinoff, J., 1998. Origin of Platinum Group Minerals in the Las Águilas Mafic-Ultramafic Intrusion, San Luis Province, Argentina. IV Reunión de Mineralogía y Metalogenia y IV Jornadas de Mineralogía, Petrografía, Metalogénesis de Rocas Máficas y Ultramáficas, Actas: 285–289, Argentina.

Pankhurst, R.J., Rapela, C.W., 1998. The proto-Andean margin of Gondwana: an introduction. In: Pankhurst, R.J., Rapela, C.W. (Ed.), The Proto-Andean Margin of Gondwana. Geological Society, London, Special Publication 142: 1–9.

Pankhurst, R. J., Rapela, C. W., Saavedra, J., Baldo, E., Dahlquist, J., Pascua, I. and Fanning, C. M., 1998. The Famatinian magmatic arc in the central Sierras Pampeanas: an Early to Mid-Ordovician arc on the Gondwana margin. In: Pankhurst, R.J., Rapela, C.W. (Ed.), The Proto-Andean Margin of Gondwana. Geological Society, London, Special Publication 142: 343–367.

Passchier, C.W., Trouw, R.A.J., 1996. Microtectonics. Springer-Verlag, Berlin, 289pp.

Pinotti, L., Coniglio, J., Llambías, E., 1996. Características geológico-estructurales del plutón Alpa Corral, 32°38′–32°47′S y 64°55′–64°45′W, Sierras Pampeanas de Córdoba, Argentina. XIII Congreso Geológico Argentino y III Congreso de Exploración de Hidrocarburos 3, 477–486.

Poirier, J.P., Nicolas, A., 1975. Deformation induced recrystallization due to progressive misorientation of subgrains, with special reference to mantle peridotites. Journal of Geology 83, 707–720.

Ramos, V.A., 1988. Late Proterozoic-Early Paleozoic of South America-a collisional history. Episodes 11 (3), 168–174.

Ramos, V., Jordan, T., Allmendinger, R., Kay, S., Cortés, J., Palma, V., 1984. Chilenia: un terreno alóctono en la evolución de los Andes centrales. XI Congreso Geológico Argentino 2, 84–106.

Ramos, V., Jordan, T., Allmendinger, R., Mpodozis, C., Cortés, J., Palma, V., 1986. Paleozoic terranes of the central Argentine-Chilean Andes. Tectonics 5, 855–880.

Ramos, V., Dallmeyer, R. D., Vujovich, G., 1998. Time constraints on the Early Palaeozoic docking of the Precordillera, central Argentina. In: Pankhurst, R. J., Rapela, C.W. (Ed.), The Proto-Andean Margin of Gondwana. Geological Society, London, Special Publication 142: 143–158.

Rapela, C., Pankhurst, R., Kirschbaum, A., Baldo, E., 1991. Facies intrusivas del Carbonífero en el batlito de Achala: evidencias de anatexia regional en las Sierras Pampeanas? XI Congreso Geológico Chileno 1, 40–43.

Rapela, C., Pankhurst, R., Casquet, R., Baldo, E., Saavedra, J., Galindo, C., Fanning, C., 1998. The Pampean Orogeny of the southern prot-Andes: Cambrian continental collision in the Sierras de Córdoba.

Sabalúa, J., Chabert, M. Santamaría, G., 1981. Mineralización de sulfuros de hierro, cobre y níquel en el cuerpo básico de las Águilas, Provincia de San Luis, VIII Congreso geológico Argentino, Actas 4: 497–507, San Luis.

Sato, A.,González, P., Llambías, E., 2002. The Ordovician of the Sierra de San Luis: Famatinian magmatic arc and low to high-grade metamorphism. In: Aceñolaza, F. (Ed.), Aspects on the Ordovician System of Argentina, Instituto Superior de Correlación Geológica, Serie Correlación Geológica 16: 327–346.

Sato, A., González, P., Llambías, E., 2003. Evolución del orógeno Famatiniano en la Sierra de San Luis: magmatismo de arco, deformación y metamorfismo de bajo a alto grado. Revista de la Asociación Geológica Argentina 58 (4), 487–504.

Schulmann, K., Mlčoch, B., Melka, R., 1996. High-temperature microstructures and rheology of deformed granite, Erzgebirge, Bohemian Massif. Journal of Structural Geology 18 (6), 719–733.

Simpson, C., De Paor, D., 1991. Deformation and kinematics of high strain zones. Structural Geology and Tectonics Division. Short Course and Notes. Annual GSA Meeting, San Diego, 116pp.

Sims, J. P., Skirrow, R. G., Stuart-Smith, P. G. and Lyons, P., 1997. Informe geológico y metalogénico de las Sierras de San Luis y Comechingones (Provincias de San Luis y Córdoba), 1:250000. Anales XXVIII, Instituto de Geología y Recursos Minerales, SEGEMAR, Buenos Aires.

Sims, J. P., Ireland, T. R., Camacho, A., Lyons, P., Pieters, P. E., Skirrow, R. G., Stuart-Smith, P. G., Miró, R., 1998. U–Pb, Th–Pb and Ar–Ar geochronolgy from the southern Sierras Pampeanas, Argentina: implications for the Palaeozoic tectonic evolution of the western Gondwana margin. In: Pankhurst, R. J., Rapela, C. W. (Ed.), The Proto-Andean Margin of Gondwana. Geological Society, London, Special Publication 142: 259–281.

Snoke, A., Tullis, J., Todd, V., 1998. Fault-related Rocks. A Photographic Atlas. Princeton University Press, Princeton, 617pp.

Spear, F.S., 1995. Metamorphic Phase Equilibria and Pressure–Temperature–Time Paths. Mineralogical Society of America, Washington, 799pp.

Stipp, M., Stünitz, H., Heilbronner, R., Schmid, S.M., 2002. The eastern Tonale Fault Zone: a "natural laboratory" for crystal plastic deformation of quartz over a temperature range from 250 to 700 °C. Journal of Structural Geology 24, 1861–1884.

Tullis, J., Yund, R.A., 1982. Grain growth kinetics of quartz and calcite aggregates. Journal of Geology 90, 301–318.

Tullis, J., Yund, R.A., 1985. Dynamic recrystallization of feldspars: a mechanism for ductile shear zone formation. Geology 13, 238–241.

Tullis, J., Yund, R.A., 1991. Diffusion creep in feldspar aggregates: experimental evidence. Journal of Structural Geology 13, 987–1000.

Twiss, R.J., Moores, E.M., 1992. Structural Geology. W. H. Freeman and Company, New York, 532pp.

Urai, J.L., 1983. Water assisted dynamic recrystallization and weakening in polycrystalline bischofite. Tectonophysics 96, 125–127.

von Gosen, W., 1998. Transpressive deformation in the southwestern part of the Sierra de San Luis (Sierrras Pampeanas, Argentina). Journal of South American Earth Sciences 11(3): 233–264.

von Gosen, W., Prozzi, C., 1996. Geology, Structure, and Metamorphism in the Area South of La Carolina (Sierra de San Luis, Argentina). XIII Congreso Geológico Argentino y III Congreso de Exploración de Hidrocarburos, Actas 2, 301–314, Buenos Aires.

von Gosen, W. and Prozzi, C., 1998. Structural evolution of the Sierra de San Luis (Eastern Sierras Pampeanas, Argentina): implications for the proto-Andean margin of Gondwana. In: Pankhurst, R. J., Rapela, C. W. (Ed.), The Proto-Andean Margin of Gondwana. Geological Society, London, Special Publication 142: 235–258.

vonGosen, W., Loske, W., Prozzi, C., 2002. New isotopic dating of intrusive rocks in the Sierra de San Luis (Argentina): implications for the geodynamic history of the Eastern Sierras Pampeanas. Journal of South American Earth Sciences 15 (2), 237–250.

White, S.H., 1976. The effects of strain on the microstructures, fabrics and deformation mechanisms in quartz. Philosophical Transactions of the Royal Society of London A283, 69–86.

Yardley, B.W.D., 1989. An Introduction to Metamorphic Petrology. Longman Scientific & Technical, New York, 248pp.